Research Square

Preprints are preliminary reports that have not undergone peer review.
They should not be considered conclusive, used to inform clinical practice,
or referenced by the media as validated information.

Tunable Spinel Ferrite Nanoparticles for High Frequency Power Magnetics and Thermal Management

R. Sagayaraj

sagayaraj@sjctnc.edu.in

St. Joseph's College of Arts and Science (Autonomous)

Systematic Review

Keywords: Spinel ferrites, Ferrite nanoparticles, Magnetic losses, High frequency magnetics, Electromagnetic interference, Thermal management

Posted Date: November 23rd, 2026

DOI: https://doi.org/10.21203/rs.3.rs-11695964/v1

License: This work is licensed under a Creative Commons Attribution 4.0 International License.
Read Full License

Additional Declarations: No competing interests reported.

Tunable Spinel Ferrite Nanoparticles for High Frequency Power Magnetics and Thermal Management

R. Sagayaraj

PG & Research Department of Physics, St. Joseph's College of Arts and Science (Autonomous), Cuddalore-607001, Affiliated to Annamalai university, Chidambaram, Tamil Nadu, India

Abstract

Soft ferrites are the material of choice for inductive cores in high frequency power electronics, and spinel ferrite nanoparticles extend their functionality to electromagnetic interference (EMI) suppression and thermal management. This critical review of the 2019–2026 literature links composition, cation distribution, and microstructure to magnetic, electrical, and thermal performance using quantitative benchmarks. Mn–Zn ferrites combine high permeability with a DC resistivity of only a few Ω m, whereas Ni–Zn ferrites exceed 10^5 Ω m, have a coercive field of 200–300 A/m instead of 5–15 A/m, and shift the permeability response by about one order of magnitude toward higher frequency. In a Mn–Zn ferrite, sintering at 1360 °C for 7 h instead of 1325 °C for 3 h increased the grain size from 11.4 to 19.8 μm and the core loss at 100 kHz by about 40%, whereas 3000–4000 ppm CoO flattened the temperature dependence of permeability and loss. At the nanoscale, the saturation magnetization of NixFe3−xO4 fell from 40.16 to 21.97 emu/g as the Ni:Fe ratio increased. The review derives a frequency map of loss mechanisms and a selection guide for Mn–Zn and Ni–Zn ferrites from published benchmarks and compares heat-management pathways on one metric: Fe_3O_4 composites raised polymer thermal conductivity by 22–46%, Fe_3O_4 ferrofluids by more than 200% under a field, while a $CoFe_2O_4$ nanofiber example showed an entropy change of 1.71 J/(kg K) near 32 K. A gap persists between material-level data and device-level metrics such as loss density at MHz frequencies. A prioritized research agenda is proposed.

Corresponding author:

R. Sagayaraj (sagayaraj@sjctnc.edu.in)

Keywords: Spinel ferrites; Ferrite nanoparticles; Magnetic losses; High frequency magnetics; Electromagnetic interference; Thermal management

1. Introduction

1.1 Background and Rationale

Ferrites are ferrimagnetic oxides that combine appreciable magnetization with high electrical resistivity, which keeps eddy-current losses low and explains their use in inductors, transformers, and other electromagnetic components [1]. Based on crystal structure they fall into four classes: spinel, garnet, hexagonal, and orthoferrites [1]. Spinel ferrites, MFe_2O_4 with M = Mg, Mn, Fe, Co, Ni, Cu, or Zn, are the most widely studied class because their magnetic properties can be tuned through the choice of divalent cation and its distribution between tetrahedral (A) and octahedral (B) sites [1].

In the spinel lattice, antiparallel alignment of the A and B sublattices, combined with twice as many B as A sites, leaves a net magnetic moment, which is the origin of ferrimagnetism [1]. At the nanoscale, size effects add further tunability: particles with diameters below roughly 3–50 nm, depending on the material, become superparamagnetic [1], and nanomaterials are conventionally defined by dimensions of 1–100 nm [2]. Spinel ferrites also show direct optical band gaps of about 1.7–4.0 eV from Tauc analysis [1], which illustrates the breadth of functionality available within one structural family.

1.2 Power Magnetics and Magnetic Losses

Sintered soft ferrites are the main material for high-frequency inductor cores because of an established and inexpensive preparation technology, compact core shapes, and low energy losses [3], and the foundations are covered by the classic monographs [4, 5]. The two dominant families differ sharply. Mn–Zn ferrites have a DC resistivity of only a few Ω m (6.3 Ω m for the commercial EPCOS N87 grade), which falls by more than one order of magnitude on reaching the MHz range, whereas Ni–Zn ferrites exceed 10^5 Ω m, so that eddy-current losses can be neglected [3]. The anisotropy constant ranges from about 10–100 J/m³ in Mn–Zn ferrites to a few kJ/m³ in Ni–Zn ferrites, and the coercive field from 5–15 A/m to 200–300 A/m [3]. Consequently the permeability of Ni–Zn ferrites extends to an order of magnitude higher frequency, in line with Snoek's relation between initial permeability and cutoff frequency [6];

the real permeability of a commercial Ni–Zn grade (Ferroxcube 4C65) peaks near 15 MHz compared with a few hundred kHz for Mn–Zn, and Ni–Zn ferrites are preferred where operating frequencies reach or exceed 10 MHz [3].

Processing and doping matter as much as composition. For a Mn–Zn ferrite made from 70 wt% Fe_2O_3, 24 wt% MnO, and 6 wt% ZnO with NbO_2 and CaO additions, lengthening the sintering schedule from 1325 °C for 3 h to 1360 °C for 7 h enlarged the average grain size from 11.4 to 19.8 μm and raised the core loss at 100 kHz and 100 mT by about 40%, while the loss minimum stayed at about 90 °C [3]. Additions of 3000–4000 ppm CoO produced the weakest temperature dependence of permeability and loss between −20 and 130 °C, and the loss minimum at 80–100 °C coincides with the typical working temperature of inductive components in power electronics [3]. Because ferrites also have a low thermal conductivity, smaller cores and higher frequencies can cause thermal drift of the magnetic response [3].

1.3 Synthesis and Property Tuning

The synthesis route and post-treatment determine particle size, phase purity, and cation distribution. Co-precipitation is typically run at about 80 °C for 1 h at pH 11–12 and followed by calcination at 500 °C for 6 h [2]; solvothermal synthesis uses 200 °C for 24 h in an autoclave [2]; microwave-assisted synthesis operates at 100–200 °C with much shorter reaction times [1]; and ceramic and solid-state routes require more than 800 °C, with calcination at 1000 °C for up to 72 h [1]. High-energy ball milling yields nanoferrites of about 35–85 nm [1]. Composition also changes the magnetic response directly: in NixFe3−xO4 samples roasted at 1200 °C for 2 h, the saturation magnetization decreased from 40.16 to 37.96 emu/g as the Ni:Fe ratio rose from 1:4 to 2:4 and dropped to 21.97 emu/g at higher ratios, whereas the coercivity increased from 89.71 to 153.09 Oe and the Ms/Mr ratio decreased from 7.05 to 3.77 [1].

1.4 Thermal Management and Solid-State Cooling

Heat removal is a growing constraint for compact electronic and power devices, and ferrites contribute to several complementary strategies [7–13]. These include ferrite-filled polymer thermal interface materials and phase-change composites [14–20], magnetic nanofluids and thermoelectric modules [21–24], and magnetocaloric refrigeration, which offers solid-state cooling without greenhouse gases [25–30]. Quantitative thermal metrics for ferrite systems, such as conductivity enhancement, interfacial thermal resistance, and adiabatic temperature change,

are reported far less often than magnetic properties, which is why Section 7 compares these pathways mainly qualitatively.

1.5 Research Gap

Most studies characterize isolated properties of a single composition, and direct comparison between studies is hindered by differing measurement conditions. The ranking of materials can even reverse with frequency: the commercial Ni–Zn grade 4C65 showed more than one order of magnitude higher loss than the Mn–Zn grade N87 at low frequency, yet its loss became persistently lower above about 1 MHz [3]. Device-level metrics such as conversion efficiency, loss density at MHz frequencies, and thermal resistance are rarely linked to composition and microstructure, and semiconductor-compatible low-temperature processing remains unresolved.

1.6 Objectives and Scope of This Review

This review (i) classifies the synthesis routes and compositions of spinel ferrite nanoparticles, (ii) relates cation distribution, composition, and microstructure to saturation magnetization, coercivity, permeability, anisotropy, Curie temperature, and magnetic loss, (iii) compares ferrite systems for high-frequency power magnetics and EMI suppression, (iv) assesses ferrite-based thermal-management pathways on a common metric, and (v) identifies the gaps and the reporting standards needed to move from material-level characterization to device-level performance. Biomedical, catalytic, and sensing uses of ferrites are outside the scope.

Recent work covers the synthesis, structure, and broad applications of spinel ferrites [1] and gives a detailed analysis of magnetic losses in commercial soft ferrites [3]. This review differs in three respects. First, it joins nanoparticle-level structure–property data with core-level loss data in one quantitative framework. Second, it derives frequency-resolved and temperature-resolved selection guidance for Mn–Zn and Ni–Zn ferrites from published benchmarks (Section 6.4). Third, it compares ferrite-based heat-management pathways on one metric, the reported enhancement of thermal conductivity (Section 7.5). It does not claim systematic coverage; its contribution is this quantitative synthesis.

2. Scope and Literature Selection

2.1 Literature Selection

This is a critical, quantitative review rather than a systematic review. Peer-reviewed literature published between 2019 and 2026 on ferrite magnetic nanoparticles and their use in power magnetics, electromagnetic interference suppression, and thermal management was collected from Scopus, Web of Science, ScienceDirect, IEEE Xplore, and SpringerLink. These sources were complemented by foundational works on ferrite physics and processing [4, 6], [5]. Numerical values are quoted only from studies that state them explicitly together with their measurement or processing conditions.

2.2 Data Handling

Quantities are reported as published, in the units used by the source. Derived statements, such as the frequency ranges in which a loss mechanism or a ferrite family is favored, are limited to values stated in the cited sources and are identified as derived from them. Where a value comes from a single study, the text says so.

3. Overview of the Literature

3.1 Publication Trends and Study Types

The literature search identified a substantial body of research investigating ferrite magnetic nanoparticles for advanced electronic, magnetic, and thermal applications of ferrite magnetic nanoparticles. Following the selection described in Section 2, the reviewed literature comprised peer-reviewed studies published between **2019 and 2026**, representing significant advances in ferrite nanomaterials for sustainable electronics. The selected publications covered diverse aspects of ferrite research, including synthesis, crystal structure, magnetic behavior, electrical transport, dielectric properties, thermal conductivity, magnetocaloric performance, power electronics, and solid-state cooling.

Table 1 and Figure 1 give the distribution of the publication years of the cited literature.

Table 1. Publication years of the references cited in this review (computed from the reference list).

Publication year	References (n)	Share (%)
1948	1	0.5
1959	1	0.5

2006	1	0.5
2012	1	0.5
2013	1	0.5
2017	1	0.5
2018	1	0.5
2019	17	9.2
2020	12	6.5
2021	29	15.7
2022	22	11.9
2023	19	10.3
2024	39	21.1
2025	35	18.9
2026	5	2.7
Total	185	100

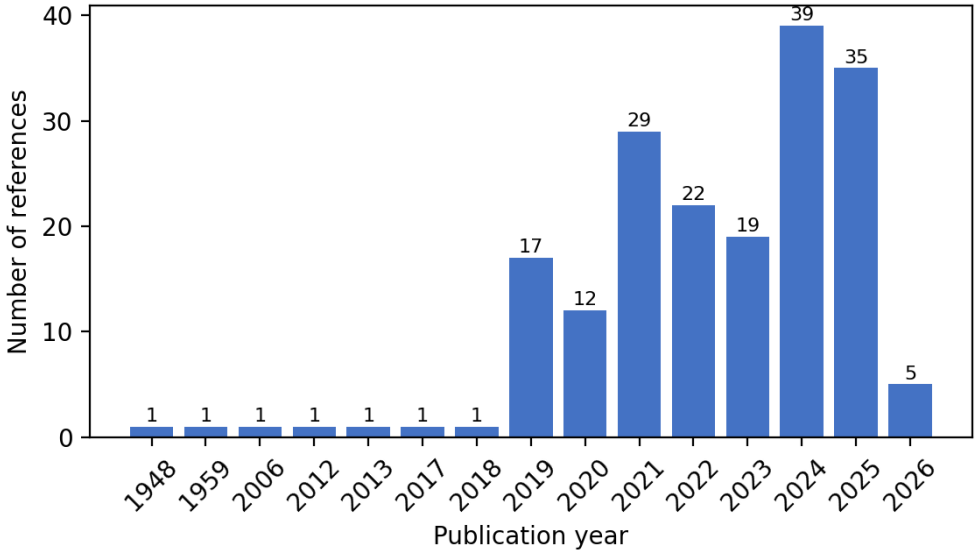

Figure 1. Publication years of the references cited in this review (computed from the reference list).

Table 1 and Figure 1 show that the cited literature is concentrated in recent years: 149 of the 185 references (81%) were published in 2021 or later, and the largest numbers date from 2024 (39) and 2025 (35). The numerical benchmarks used in Sections 5 to 7 therefore rest mainly on current work, while the few older references are the foundational monographs and papers cited for the underlying physics.

The literature demonstrates a marked increase in research activity during the review period, reflecting the growing demand for multifunctional materials capable of addressing the energy efficiency and thermal management requirements of next-generation electronic systems. Although ferrite nanoparticles have traditionally been investigated for magnetic recording, microwave devices, transformers, and electromagnetic interference (EMI) suppression, recent studies have increasingly focused on their integration into electronic hardware, including high-

frequency power converters, integrated inductors, voltage regulators, thermal interface materials, and magnetic refrigeration systems. Experimental studies have primarily explored composition engineering, nanostructure control, synthesis optimization, and structure–property relationships, whereas computational investigations have focused on magnetic exchange interactions, thermal transport mechanisms, electronic band structures, and device-level performance simulations.

Ferrite magnetic nanoparticles (MFe_2O_4) can be synthesized using a diverse range of methods, each offering unique benefits in controlling particle size, morphology, crystallinity, cation distribution, magnetic properties, and scalability. These methods, as illustrated in Figure 3, are broadly categorized into chemical routes, including co-precipitation, sol–gel auto-combustion, citrate precursor, combustion synthesis, chemical vapor deposition, spray pyrolysis, and pulsed laser deposition, hydrothermal/solvothermal techniques, physical approaches such as mechanical alloying and electrospinning, microwave-assisted synthesis, and green synthesis utilizing plant extracts.

Table 2 and Figure 2 summarize the temperatures reported for each route.

Table 2. Synthesis conditions reported for spinel ferrite nanoparticles. Data from [2] and [1]. A dash means that no value was reported in the cited text.

Method	Reported processing conditions	Reported size	Source
Co-precipitation	60–80 °C; 1 h at 80 °C, pH 11–12; calcination 500–600 °C (6–10 h)	Size set by calcination ($NiFe_2O_4$ annealed at 400–800 °C, 4 h)	[1, 2]
Combustion (sol–gel auto-combustion)	Gel at 70–80 °C; self-ignition at 170–180 °C (≈ 5 min); anneal 300–1000 °C, 4 h	—	[1, 2]
Sol–gel	Calcination 300–450 °C ($NiFe_2O_4$, $ZnFe_2O_4$); $MnFe_2O_4$: 900 °C, 2 h, then sintering 1200 °C, 3 h	—	[2]
Thermal decomposition	300 °C, 1 h ($NiFe_2O_4$); $Fe(acac)_3$ route up to 265 °C	Magnetite up to 20 nm	[2]
Hydrothermal / solvothermal	200 °C, 24 h in a Teflon-lined autoclave	—	[1, 2]
Microwave-assisted	100–200 °C; short reaction times (10 min at 100 °C in one example)	—	[1, 2]
Electrochemical	60 °C, 30 min, 50 and 100	—	[2]

	mA anode currents		
Sonochemical	0–30 °C, 3 h of ultrasonic irradiation (carbonyl precursors); no calcination	—	[1, 2]
Ceramic / solid-state	> 800 °C; 1000 °C for up to 72 h; $ZnFe_2O_4$ 1200 °C for 2 days	Grains ≈ µm ($LiMg_{0.5}Fe_2O_4$: 2.27 µm)	[1, 2]
High-energy ball milling	Solid-state mechanical processing	35–85 nm	[1]

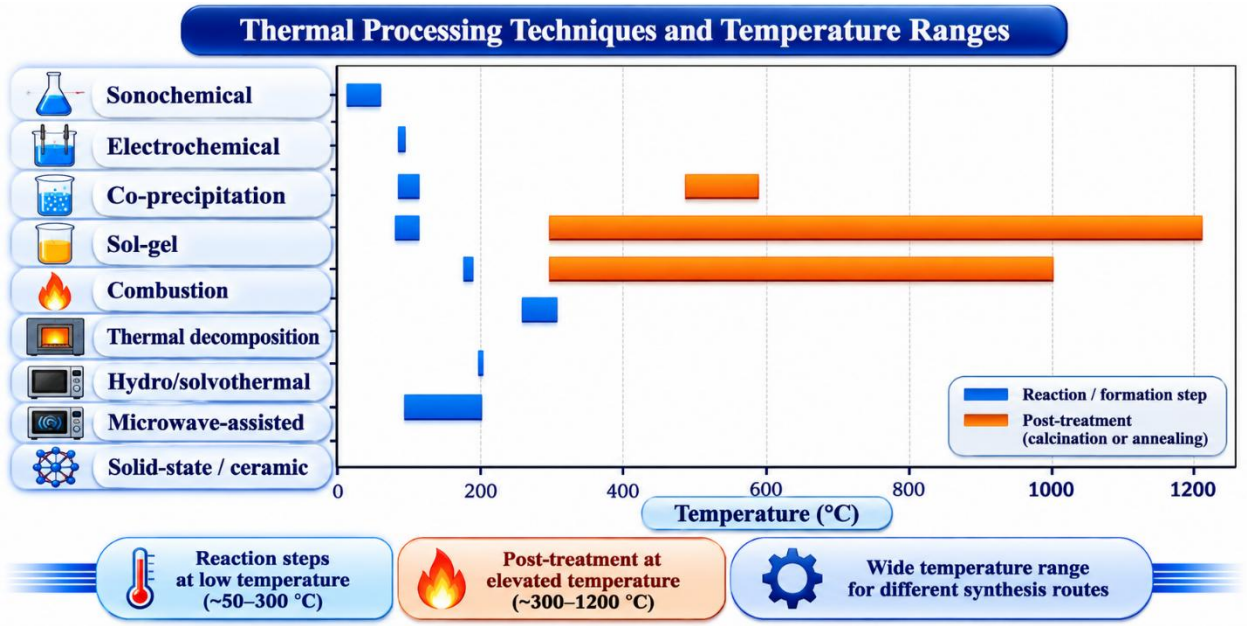

Figure 2. Temperature ranges reported for the formation step and for post-treatment of the main synthesis routes. Data from [2] and [1] (Table 2).

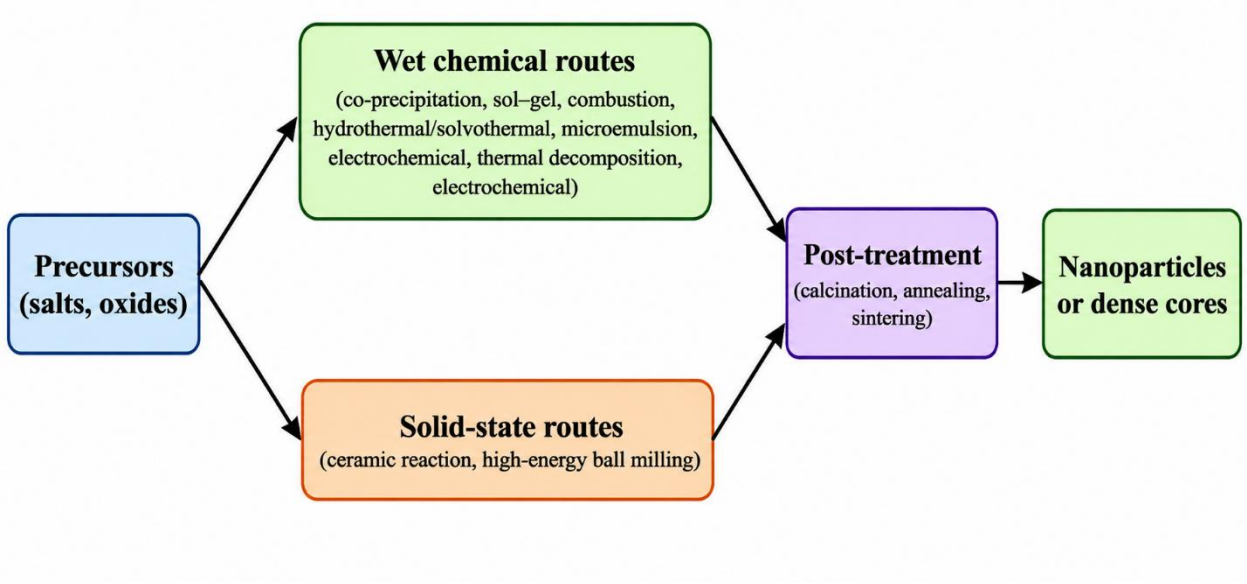

Figure 3. Overview of the synthesis routes for ferrite nanoparticles and cores. Routes and conditions follow [2] and [1]; drawn by the authors.

Table 2, Figure 2, and Figure 3 link the synthesis route to the temperature budget. Wet-chemical routes form the ferrite at about 0–300 °C (sonochemical 0–30 °C, co-precipitation 60–80 °C, solvothermal 200 °C, thermal decomposition up to 300 °C) but usually need calcination at about 300–600 °C for crystallinity, whereas solid-state routes work directly above 800 °C (1000–1200 °C). Because the Mn–Zn cores of power magnetics are sintered at about 1325–1360 °C (Table 9), the choice of route decides whether nanoscale features survive in dense cores, and this processing–structure link is the starting point of the property sections that follow.

3.2 Ferrite Systems Investigated

The selected publications cover a broad spectrum of spinel ferrite compositions, each exhibiting unique combinations of magnetic, electrical, and thermal properties suitable for specific power-electronics and thermal-management applications, as summarized in **Table 3**. The table highlights various spinel ferrite compositions that have been extensively studied for their distinct magnetic, electrical, and thermal properties, making them suitable for specific power-electronics and thermal-management applications. For instance, $MgFe_2O_4$ is valued for its soft magnetic behavior and thermal stability, which are critical for high-frequency inductors, whereas the high permeability of $NiFe_2O_4$ makes it ideal for power converters. $ZnFe_2O_4$ exhibits notable dielectric behavior, making it suitable for sensors and energy storage devices. $CoFe_2O_4$, known for its high coercivity, is primarily applied in magnetic memory technologies, whereas the high saturation magnetization of $MnFe_2O_4$ supports wireless power transfer systems. $CuFe_2O_4$ is distinguished by its electrical conductivity, making it suitable for various electronic devices. Mixed ferrite systems, such as Mg–Zn, Ni–Zn, and Mn–Zn ferrites, offer tailored properties, such as low magnetic loss, high-frequency operation, and transformer core functionality, which are essential for integrated voltage regulators, DC–DC converters, and power modules. Additionally, rare-earth-doped ferrites provide opportunities for fine-tuning the material properties to meet the demands of advanced electronic systems.

Table 3. Spinel ferrite compositions in the reviewed literature, their major research focus, and potential applications.

Ferrite composition	Major research focus	Potential applications	Reference
$MgFe_2O_4$	Soft magnetism, thermal stability	High-frequency inductors	[31, 32]

$NiFe_2O_4$	High permeability	Power converters	[33]
$ZnFe_2O_4$	Dielectric behavior	Sensors and energy storage	[34–37]
$CoFe_2O_4$	High coercivity	Magnetic memory	[38]
$MnFe_2O_4$	High saturation magnetization	Wireless power transfer	[39]
$CuFe_2O_4$	Electrical conductivity	Electronic devices	[40–42]
Mg–Zn ferrites	Low magnetic loss	Integrated voltage regulators	[43]
Ni–Zn ferrites	High-frequency operation	DC–DC converters	[44–47]
Mn–Zn ferrites	Transformer cores	Power modules	[48–51]
Rare-earth-doped ferrites	Property tuning	Advanced electronics	[52–55]

Table 3 pairs each composition with its dominant property and application: Mg and Mg–Zn ferrites with low loss, Ni and Ni–Zn ferrites with high-frequency operation, Mn and Mn–Zn ferrites with high saturation magnetization and transformer cores, and Co ferrite with high coercivity. These pairings are tested against measured benchmarks in Table 10 and Table 12.

4. Structural Characteristics and Tunability of Ferrite Nanoparticles

4.1 Crystal Structure of Spinel Ferrites

Ferrite magnetic nanoparticles are among the most versatile inorganic functional materials owing to their unique spinel crystal structure, exceptional compositional flexibility, and multifunctional properties. Most technologically important ferrites possess a cubic spinel structure with the general chemical formula MFe2O4. where **M** represents a divalent metal cation, such as Mg^{2+}, Mn^{2+}, Zn^{2}, Ni^{2+}, Co^{2}, Cu^{2}, or a combination of these ions. The crystal structure belongs to the **$Fd\bar{3}m$** space group and consists of a face-centered cubic (FCC) arrangement of oxygen anions[56–58], within which metal cations occupy two crystallographically distinct interstitial sites:

Table 4, Figure 4, and Figure 5 summarize the four ferrite classes and the spinel crystal structure.

Table 4. Classification of ferrites by crystal structure. The classification follows [1]; general formulas and typical roles are standard crystal-chemistry descriptions.

Class	General formula	Structure	Typical role
Spinel	MFe_2O_4 (M = Mg, Mn, Fe, Co, Ni, Cu, Zn)	Cubic; oxygen close-packed array with tetrahedral (A) and octahedral (B) cation sites	Soft magnetic cores, EMI suppression, sensors, catalysis (focus of this review)
Garnet	$R_3Fe_5O_{12}$	Cubic; three cation coordinations	Microwave and magneto-optical devices

Hexagonal (hexaferrite)	$MFe_{12}O_{19}$ (M = Ba, Sr)	Hexagonal magnetoplumbite	Permanent magnets and high-frequency absorbers
Orthoferrite	$RFeO_3$	Distorted perovskite	Magnetic and magneto-optical research

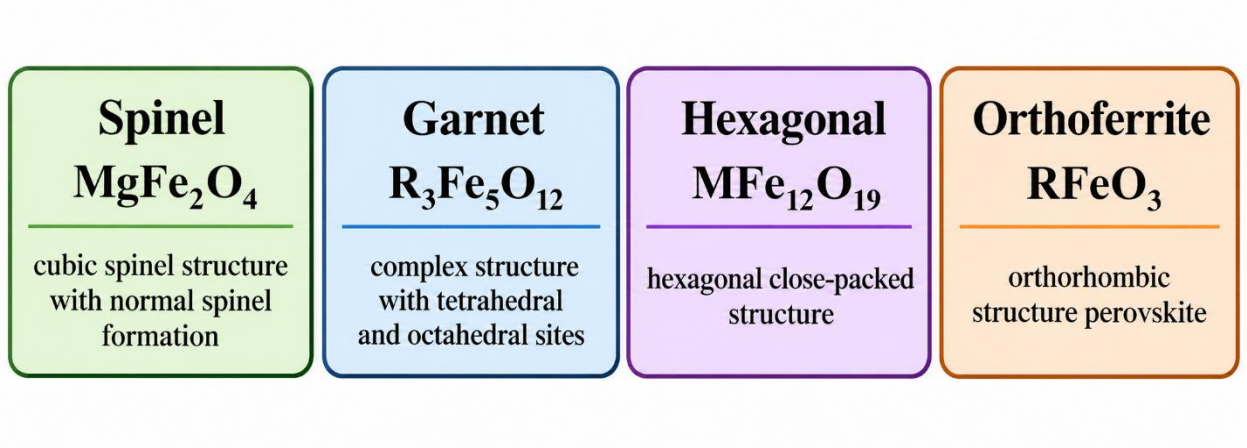

Figure 4. The four classes of ferrites: spinel, garnet, hexagonal, and orthoferrite. Classification follows [1]; schematic drawn by the authors.

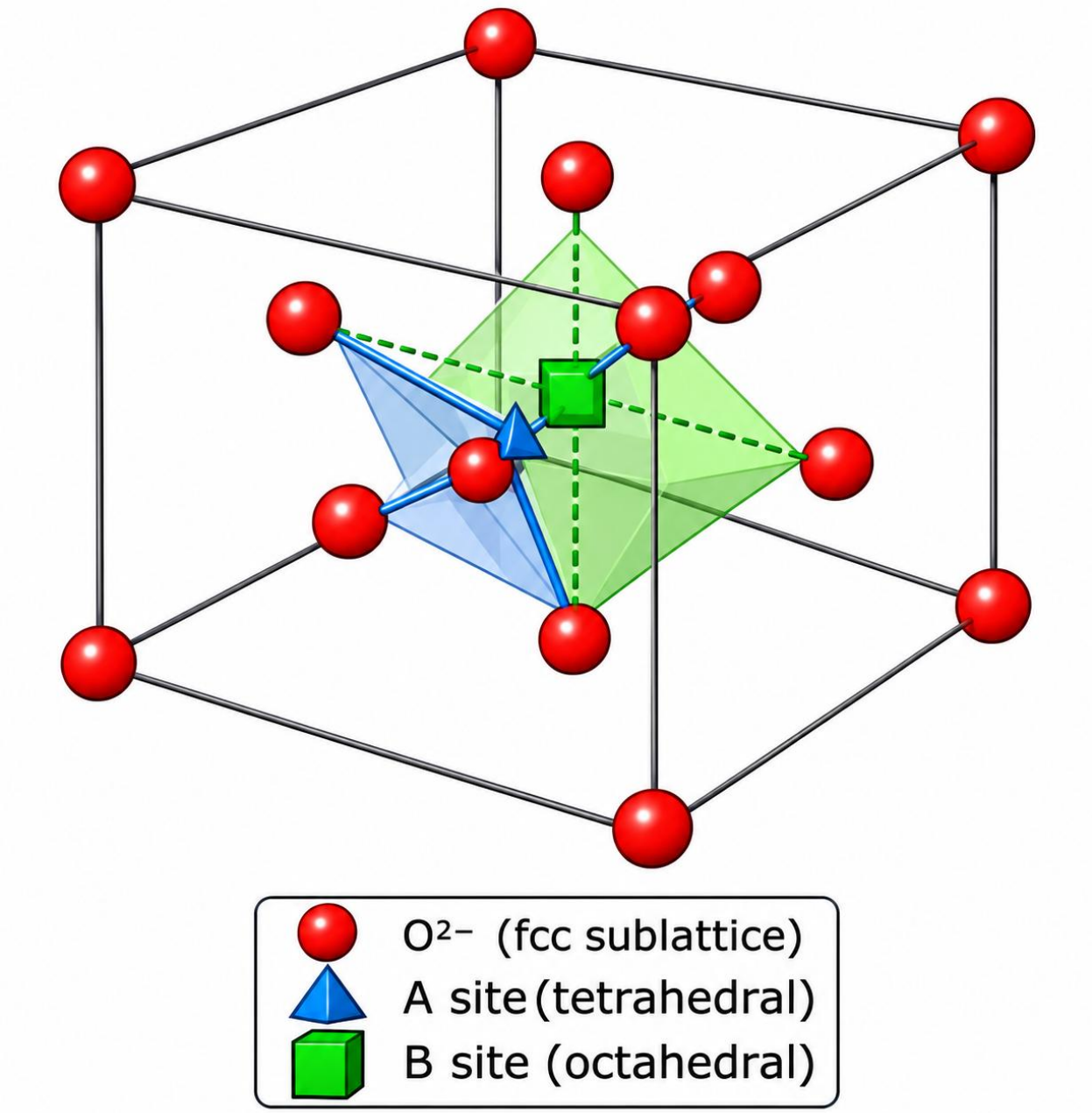

Figure 5. Schematic of the spinel structure: one cube of the face-centered-cubic oxygen sublattice with one tetrahedral (A) and one octahedral (B) interstitial site. Site types follow [1]; drawn by the authors.

Table 4, Figure 4, and Figure 5 place spinel ferrites among the four ferrite classes and show why they are the focus of this review: the spinel structure combines a cubic oxygen sublattice with two cation site types, tetrahedral A and octahedral B, and these sites are the tuning parameters discussed next. Garnets and hexagonal ferrites serve other roles (microwave devices and permanent magnets) and are outside the scope.

Table 5 and Figure 6 summarize the three cation-distribution types and their magnetic consequence.

Table 5. Cation-site occupancy in spinel ferrites. Site descriptions follow [1]; the example compounds are the usual textbook examples.

Spinel type	Tetrahedral (A) sites	Octahedral (B) sites	Typical example	Magnetic consequence
Normal	Me^{2+}	Fe^{3+}	$ZnFe_2O_4$	Antiparallel A/B coupling; twice as many B as A sites leaves a net moment
Inverse	Fe^{3+}	Fe^{3+} and Me^{2+} shared	$NiFe_2O_4$	Tuned by the type and distribution of Me^{2+}
Partially inverse (mixed)	Me^{2+} and Fe^{3+}	Me^{2+} and Fe^{3+}	Many mixed ferrites	Properties depend on the degree of inversion

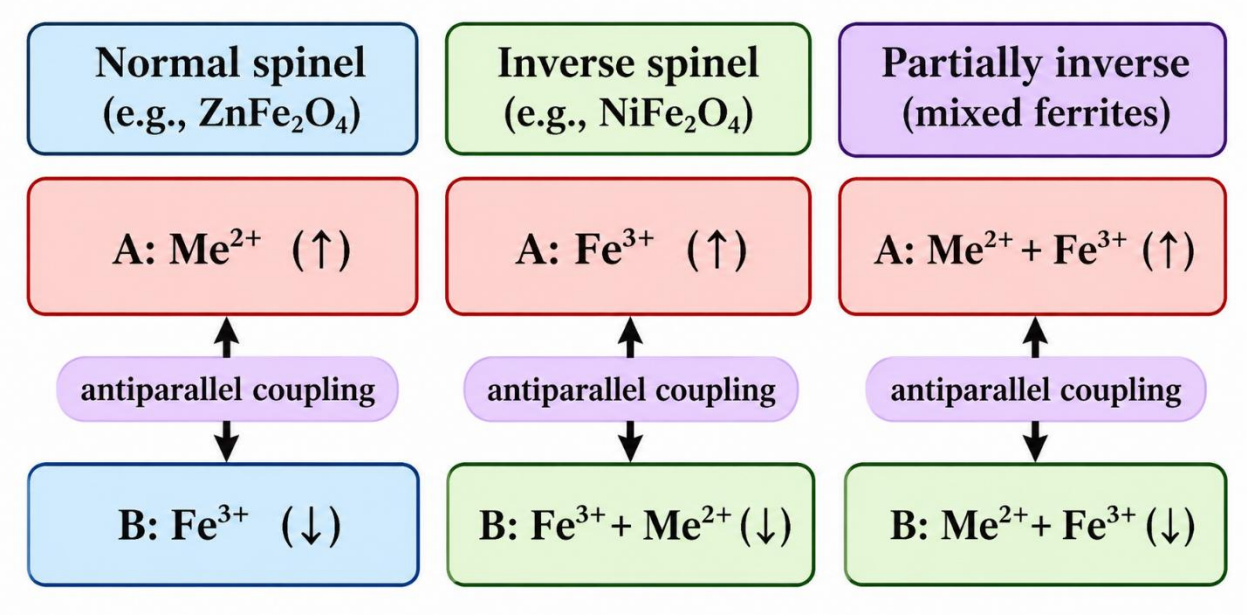

Figure 6. Schematic of cation occupancy in normal, inverse, and partially inverse spinel ferrites. Site descriptions follow [1].

Table 5 and Figure 6 show that the type of site occupancy decides the net moment: in the normal spinel the Me^{2+} ions occupy A sites and Fe^{3+} ions B sites, in the inverse spinel Fe^{3+} fills all A sites and Me^{2+} shares the B sites, and real ferrites are often partially inverse. Because the A and B moments couple antiparallel and B sites are twice as numerous, changing the cation distribution changes the saturation magnetization (Section 5.1), the superexchange coupling, and the Curie temperature (Section 5.5).

- **Tetrahedral (A) sites**

- **Octahedral (B) sites**

The distribution of cations between these sites determines the magnetic, electrical, dielectric, optical, and thermal characteristics of the ferrite nanoparticles[56, 59]. Unlike many conventional magnetic materials, ferrites exhibit remarkable compositional flexibility, allowing the controlled substitution of multiple cations without disrupting the spinel framework. This flexibility renders ferrites particularly attractive for electronic hardware, where multifunctional optimization is required. **Figure 5 illustrates the crystal structure** of spinel ferrites with the general formula MFe_2O_4. The figure illustrates the oxygen framework that constitutes the lattice and the superexchange interactions that occur between cations via oxygen ions. In these configurations of cations at the A (tetrahedral) and B (octahedral) sites, the ionic radii result in materials displaying three distinct structural characteristics: normal, inverse, and mixed spinel structures[59]. In normal spinels((M^{2+}) A $[Fe^{3+}Fe^{3+}]$ BO_4), divalent cations occupy the tetrahedral sites, whereas Fe^{3+} ions occupy the octahedral sites. Examples of normal spinels include $ZnFe_2O_4$ and $CdFe_2O_4$. These ferrites generally exhibit lower magnetic ordering because the strongest magnetic interactions occur between the A and B sites[60–62].

Inverse spinels($(Fe^{3+})A[M^{2+}Fe^{3+}]BO^4$) exhibit a different cation distribution, where Fe^{3+} ions occupy the tetrahedral sites and divalent cations occupy half of the octahedral positions. Examples of inverse spinels include $NiFe_2O_4$ and $CoFe_2O_4$. This cation arrangement often results in a higher saturation magnetization and stronger exchange interactions than normal spinels, making inverse spinels particularly significant in magnetic applications[59, 63]. Most technologically useful ferrites fall into the mixed-spinel category($(M_{1-\delta}Fe_\delta)A[M_\delta Fe_{2-\delta}]B]$ O_4), where cations are distributed between both tetrahedral and octahedral sites according to an inversion parameter (δ). This distribution is represented as $(M^{1-\delta}Fe^{\delta})_a[M^{\delta}Fe_2^{-\delta}]_\beta O_4$. Examples include $MgFe_2O_4$, $MnFe_2O_4$, and various Mg–Zn, Ni–Zn, and Mn–Zn ferrites. Mixed spinels are particularly attractive because the inversion parameter δ can be controlled through the synthesis conditions, annealing temperature, particle size, and dopant concentration, enabling precise tuning of their multifunctional properties[59, 60, 64, 65].

4.2 Magnetic Exchange Interactions

The magnetic properties of ferrites primarily arise from superexchange interactions mediated by oxygen ions, as shown in Figure 5. These interactions occur in three forms: A–O–A, B–O–B,

and A–O–B, with the A–O–B superexchange interaction being the strongest and most influential in determining the overall magnetic order. This exchange mechanism can be represented as Fe^{3+}–O^{2-}–M^{2+}, where the oxygen ions serve as intermediaries facilitating indirect magnetic coupling between the cations. The net magnetic moment (M_net) is approximately the difference between the magnetic moments of the octahedral (MB) and tetrahedral (MA) sublattices, expressed as M_net = MB − MA[66–70]. Changes in cation distribution directly affect key magnetic parameters, such as the saturation magnetization, coercivity, Curie temperature, permeability, and magnetic anisotropy. In the context of electronic hardware, optimizing the A–B exchange interactions is critical for enhancing performance characteristics, including achieving high magnetic permeability, minimizing hysteresis loss, enabling efficient operation at high frequencies, and reducing magnetic heating[71, 72].

4.3 Cation Distribution Engineering

One of the most powerful approaches for tuning ferrite performance involves engineering the cation occupancy within the spinel lattice. Cation redistribution may be achieved through various factors, such as annealing temperature, cooling rate, dopant concentration, oxygen partial pressure, particle size, hydrothermal pressure, and chemical precursor selection. Thermal treatment often drives cations toward equilibrium distributions, whereas low-temperature synthesis tends to produce metastable arrangements. For example, increasing the annealing temperature frequently promotes the migration of Zn^{2+} ions toward tetrahedral sites, whereas Fe^{3+} ions redistribute toward octahedral positions[73, 74]. This redistribution influences the exchange interactions, magnetocrystalline anisotropy, dielectric polarization, electrical conductivity, and thermal conductivity. The ability to engineer cation occupancy provides exceptional flexibility in designing high-frequency magnetic materials.

4.4 Defect Engineering

Real ferrite nanoparticles often deviate from ideal crystal structures owing to the presence of various defects. These defects include oxygen vacancies, cation vacancies, antisite defects, lattice strain, grain boundaries, dislocations, and surface disorder. While defects are commonly perceived as detrimental to material properties, controlled defect engineering can enhance the multifunctional behavior of ferrite nanoparticles, improving their overall performance in targeted

applications[75]. Oxygen vacancies play a critical role in influencing several key properties of ferrite nanoparticles. These defects affect electron hopping mechanisms, dielectric polarization, electrical conductivity, and magnetic coupling. When the oxygen vacancy concentrations are maintained at moderate levels, they can enhance the electrical transport properties without compromising the magnetic ordering, thereby optimizing the balance between conductivity and magnetism[76]. The lattice strain within the ferrite nanoparticles alters the fundamental structural parameters, such as bond lengths and bond angles, which in turn affect the exchange interactions and phonon transport. This internal strain can be deliberately manipulated using strain engineering techniques, providing an effective approach to optimize the magnetocaloric performance. By tuning these strain-induced modifications, the thermal and magnetic responses of the nanoparticles can be significantly improved[77, 78]. Surface disorder is another important factor owing to the high surface area-to-volume ratio of nanoparticles. Surface spin disorder strongly influences the magnetic behavior of ferrite nanoparticles, often leading to their instability. To mitigate these effects, surface modification strategies using materials such as silica, polymers, graphene, carbon nanotubes, and organic ligands have been employed. These coatings reduce surface defects and enhance magnetic stability, contributing to the improved functionality and durability of the nanoparticles[79, 80].

4.5 Particle Size Effects

Particle size is a fundamental parameter that significantly influences the performance of ferrite materials. Typically, ferrite nanoparticles range from 5 to 100 nm; however, the synthesis conditions often lead to the formation of larger agglomerates. The size of these particles directly affects various physical properties, including the magnetic domain structure, coercivity, saturation magnetization, dielectric constant, thermal conductivity, and surface energy, all of which are critical to the functionality of the material in different applications[66, 81]. When the particle size falls below a critical diameter, the ferrite particles enter the single-domain regime. In this regime, particles exhibit fast magnetization reversal, low hysteresis, and reduced magnetic loss, making these characteristics highly desirable for GHz-frequency inductor applications. The single-domain nature ensures stable and efficient magnetic behavior, which is essential for high-frequency performance and energy-efficient device operation[82, 83]. Further reduction in the particle size leads to superparamagnetic behavior, characterized by negligible coercivity, zero remanence, and rapid magnetic response. While superparamagnetism is beneficial for biomedical

applications owing to its responsiveness and lack of residual magnetization, it is generally unfavorable for magnetic core applications that require stable and persistent magnetization. Therefore, controlling the particle size to avoid superparamagnetism is crucial for maintaining the desired magnetic properties for such applications[84–86]. Grain growth, which is promoted by higher annealing temperatures, improves the crystallinity, reduces defects, and strengthens the exchange interactions within ferrite materials. However, excessive grain growth can create longer eddy current pathways, which degrade the high-frequency performance by increasing losses. Consequently, optimizing the particle size involves balancing grain growth to enhance the material quality without compromising the magnetic performance at high frequencies, making it a critical design consideration in ferrite synthesis and applications [68].

4.6 Morphology Engineering

Nanoparticle morphology significantly impacts their multifunctional properties, complementing the influence of particle size. Various morphologies have been reported, including spherical nanoparticles, nanocubes, nanorods, nanofibers, nanosheets, hollow spheres, porous particles, and core-shell structures[87]. Each morphology imparts distinct physical and chemical characteristics that can be tailored for specific applications in fields such as catalysis, electronics and biomedicine. **Figure 7 shows the surface structure** and particle distribution of the synthesized nanoparticles, highlighting their uniformity and nanoscale size.

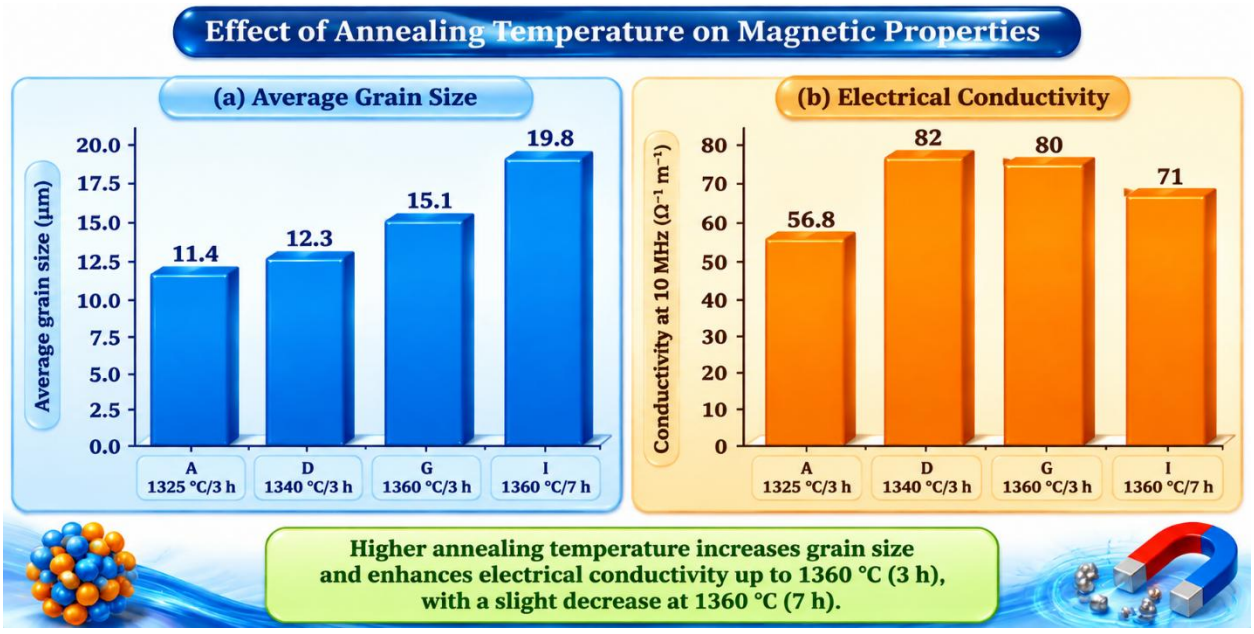

Figure 7. Average grain size and conductivity at 10 MHz of Mn–Zn ferrite rings sintered under different schedules. Replotted from the data in [3].

Figure 7 shows the processing–microstructure–property chain for a Mn–Zn ferrite: raising the sintering schedule from 1325 °C for 3 h (sample A) to 1360 °C for 7 h (sample I) enlarged the grain size from 11.4 to 19.8 μm, while the conductivity at 10 MHz varied between 56.8 and 82 Ω^{-1} m^{-1} and was highest for sample D. A larger grain means fewer insulating grain boundaries per unit length, which is the usual explanation for the higher DC conductivity of samples D, G, and I (0.214–0.220 Ω^{-1} m^{-1}) than of sample A (0.146 Ω^{-1} m^{-1}), and a higher conductivity raises the eddy-current contribution at MHz frequencies (Table 11). The full parameter set is given in Table 9.

Additionally, their structure contributes to improved mechanical strength and flexibility, making them suitable for flexible electronic devices and composite materials that require durability and adaptability. The elongated shape of the nanofibers facilitates these advantages by allowing interconnected networks within the matrix[88–92]. Hollow structures offer unique benefits, such as reduced density, which is advantageous for lightweight applications. They also improve heat transfer owing to their increased surface area and facilitate larger specific surface areas that enhance reactivity and adsorption capabilities. These properties make hollow nanoparticles ideal for use in catalysis, drug delivery, and thermal management systems, where efficient heat dissipation and surface interactions are critical[93–95]. Core-shell structures, such as Ferrite@SiO_2, Ferrite@Carbon, and Ferrite@Graphene, are engineered to combine the properties of different materials at the nanoscale. These architectures improve oxidation resistance, thermal stability, and electrical insulation, and enhance interfacial heat transport. Such multifunctional enhancements make core-shell nanoparticles valuable for applications requiring robust performance under harsh environmental conditions, including energy storage, sensors, and electronic devices[96–101].

4.7 Composition Engineering

Composition engineering remains the most effective strategy for tailoring ferrite nanoparticles to meet specific device requirements. Composition engineering remains the most effective strategy

for tailoring ferrite nanoparticles to meet specific device requirements. By substituting various ions into the ferrite structure, distinct magnetic, electrical, and thermal properties can be optimized to enhance the performance of devices. For instance, Mg^{2+} ions reduce coercivity, making them suitable for high-frequency inductors, whereas Zn^{2+} increases permeability, benefiting voltage regulators[45]. Mn^{2+} enhances the saturation magnetization, making it ideal for transformer cores, and Ni^{2+} imparts a soft magnetic behavior, which is advantageous in power converters[102]. Rare-earth dopants such as Gd^{3+} enhance thermal stability, which is critical for processors, La^{3+} reduces grain growth, facilitating miniaturized components, Nd^{3+} increases anisotropy for magnetic memory applications, and Y^{3+} improves dielectric properties, aiding electromagnetic interference (EMI) suppression[103]. Through careful compositional tuning, ferrite nanoparticles can simultaneously optimize the magnetic, electrical, and thermal characteristics required for next-generation electronic systems.

Table 6 summarizes the dopant effects.

Table 6. Effects of common dopants in spinel ferrites and the components that benefit. Effects follow the authors' compilation of the reviewed literature; additives in Mn–Zn and Ni–Zn ferrites are from [3]; dopant effects are also discussed with references [45, 102], [103] in Section 4.7.

Dopant / additive	Primary effect	Relevant component or application
Mg^{2+}	Lower coercivity	High-frequency inductors
Zn^{2+}	Higher permeability	Voltage regulators
Mn^{2+}	Higher saturation magnetization	Transformer cores
Ni^{2+}	Soft magnetic behavior	Power converters, DC–DC converters
Co^{2+}	Higher anisotropy	Anisotropy tuning
CoO in Mn–Zn (3000–4000 ppm)	Weakest temperature dependence of permeability and loss from −20 to 130 °C	Inductive components at 80–100 °C working temperature
Cu^{2+}	Higher conductivity; replaces Ni^{2+} on octahedral sites in Ni–Zn for cost reasons	Integrated electronics, Ni–Zn cores
SiO_2, CaO, Nb_2O_5 (Mn–Zn)	Change the nature and resistivity of grain boundaries	Low-loss Mn–Zn cores
TiO_2, SnO_2, CoO (Mn–Zn)	Dissolve in the lattice, enter Fe^{3+} sites, modify intragrain resistivity and anisotropy	Loss and permeability tuning
Gd^{3+}	Enhanced thermal stability	Thermally demanding components
La^{3+}	Reduced grain growth	Miniaturized components
Nd^{3+}	Higher anisotropy and improved magnetic ordering	Anisotropy-engineered components
Y^{3+}	Improved dielectric properties; lower magnetic loss	EMI suppression

Table 6 groups the dopants by the property they modify: Mg^{2+} and Ni^{2+} keep the coercivity low, Zn^{2+} raises permeability, Mn^{2+} raises saturation magnetization, Co^{2+} raises anisotropy, and

additives in Mn–Zn ferrites act at the grain boundaries (SiO_2, CaO, Nb_2O_5) or inside the grains (TiO_2, SnO_2, CoO). The practical consequence is the temperature stabilization obtained with 3000–4000 ppm CoO, which ties the composition to the loss minimum at 80–100 °C (Section 5.9) and to the selection guide in Table 13.

4.8 Structure–Property Relationship

The reviewed studies consistently demonstrate that the ferrite performance is governed by a hierarchical structure–property relationship:

Composition → Crystal Structure → Cation Distribution → Defects → Microstructure → Magnetic/Electrical/Thermal Properties → Device Performance

Figure 8 shows the structure–property–performance framework used in this review, and Table 7 lists the characterization techniques and numerical signatures used to establish each link.

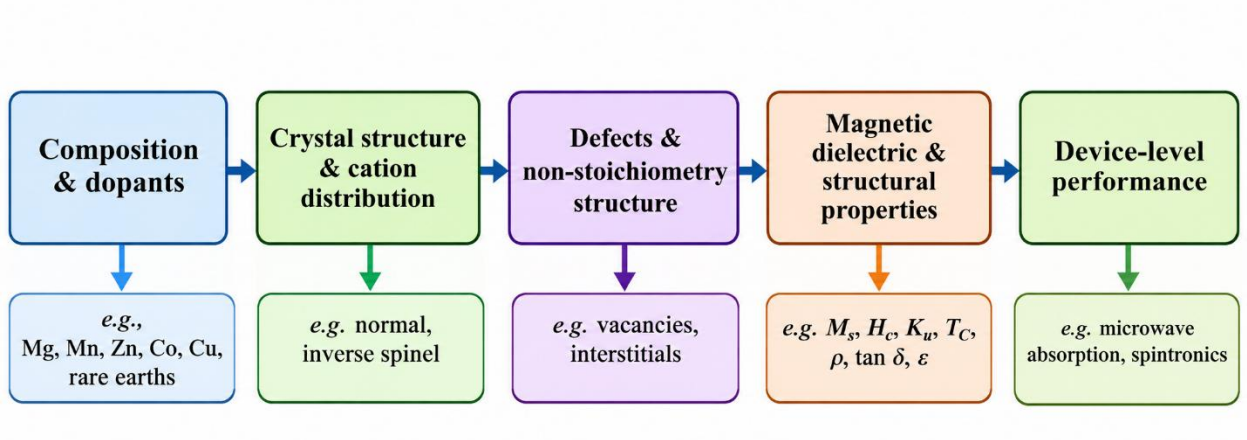

Figure 8. Structure–property–performance framework linking composition, structure, microstructure, properties, and device-level performance. Conceptual figure drawn by the authors; quantitative anchors are given in Tables 2, 10, and 11.

Table 7. Characterization techniques for spinel ferrites and the numerical signatures reported in the literature. Data from [1] and [3].

Technique	Information obtained	Reported values
X-ray diffraction	Phase, lattice parameter, crystallite size and microstrain	Debye–Scherrer $D = k\lambda/(\beta \cos \theta)$ with $k \approx 0.9$; Williamson–Hall gives slightly larger sizes
SEM / EDS	Morphology, grain size, porosity, composition	$LiMg_{0.5}Fe_2O_4$ prepared by solid-state reaction: mean grain size ≈ 2.27 µm

FTIR	Spinel confirmation by metal–oxygen stretching	≈ 600 cm^{-1} (tetrahedral) and ≈ 425 cm^{-1} (octahedral); Fe–O region 600–400 cm^{-1}
Raman	Lattice vibrations, strain, defects	≈ 200 cm^{-1} (195–206) lattice modes; 509–597 cm^{-1} Fe–O stretching; 608–705 cm^{-1} and ≈ 720 cm^{-1} bands
UV–Vis (Tauc)	Direct optical band gap	Measured over 200–800 nm; gaps ≈ 1.7–4.0 eV
Photoluminescence	Defects and oxygen vacancies	Emission bands ≈ 450–530 nm
VSM / SQUID	Ms, Hc, Mr, temperature dependence	Superparamagnetism typically below ≈ 3–50 nm
Broadband permeability and loss	Complex permeability and energy loss versus frequency	Fluxmetric up to 20 MHz; vector-network-analyzer (shorted line) from a few hundred kHz to ≈ 1 GHz

Figure 8 and Table 7 define how each link of the framework is measured: composition and structure by XRD, FTIR, and Raman, microstructure by SEM and EDS, magnetic properties by VSM or SQUID, and broadband permeability and loss by fluxmetric (up to 20 MHz) and shorted-line vector-network-analyzer (up to about 1 GHz) methods. A property reported without the matching structural data, such as size from XRD and SEM, cannot be assigned to its cause, which is the reporting gap addressed in Table 15.

5. Magnetic Property Optimization for Power-Delivery Applications

5.1 Saturation Magnetization

Saturation magnetization (Ms) is a crucial magnetic parameter that represents the maximum magnetic moment achieved when all magnetic domains are aligned under an external magnetic field. A high Ms enables a greater magnetic flux density, allowing compact inductors and transformers to store and transfer more magnetic energy. The net magnetization of spinel ferrites is given by $M_{net} = M_B - M_A$, where M_B and M_A are the magnetic moments of the octahedral and tetrahedral sublattices, respectively. Thus, changes in cation occupancy directly affect Ms. Studies have shown that increasing the crystallinity through controlled annealing generally enhances Ms by reducing structural defects, strengthening superexchange interactions, and decreasing surface spin disorder. Additionally, cation substitution with Mn^{2+} or Ni^{2+} often improves magnetic ordering, whereas excessive Zn^{2+} substitution may reduce magnetization owing to weakened A–B interactions[104–106]. The particle size also significantly influences Ms, where very small nanoparticles have a large fraction of disordered surface spins, which reduce Ms, and as the particle size increases into the single-domain regime, the magnetic ordering improves, and the saturation magnetization typically increases. However, beyond a critical size, multidomain formation and increased eddy current pathways may limit the high-

frequency performance[107]. For power-electronics and thermal-management applications, ferrites with moderate to high saturation magnetization are desirable because they are used in high-frequency inductors, integrated transformers, voltage regulator modules, wireless power transfer, and on-chip magnetic components.

Table 8 and Figure 9 illustrate how composition changes the magnetization of NixFe3−xO4. As the Ni:Fe ratio increased from 1:4 to 2:4, the saturation magnetization decreased from 40.16 to 37.96 emu/g, and it fell to 21.97 emu/g at higher ratios, which was attributed to Ni^{2+} inhibiting grain growth and to a larger fraction of non-collinear surface spins [1].

Table 8. Reported effect of the Ni:Fe molar ratio on the magnetic properties of NixFe3−xO4 roasted at 1200 °C for 2 h in air. Data from [1]. n.r. = not reported in the cited text.

Ni:Fe ratio	Ms (emu/g)	Hc (Oe)	Ms/Mr
1:4	40.16	89.71	7.05
2:4	37.96	n.r.	n.r.
> 2:4	21.97	n.r.	n.r.
4:4	n.r.	153.09	3.77

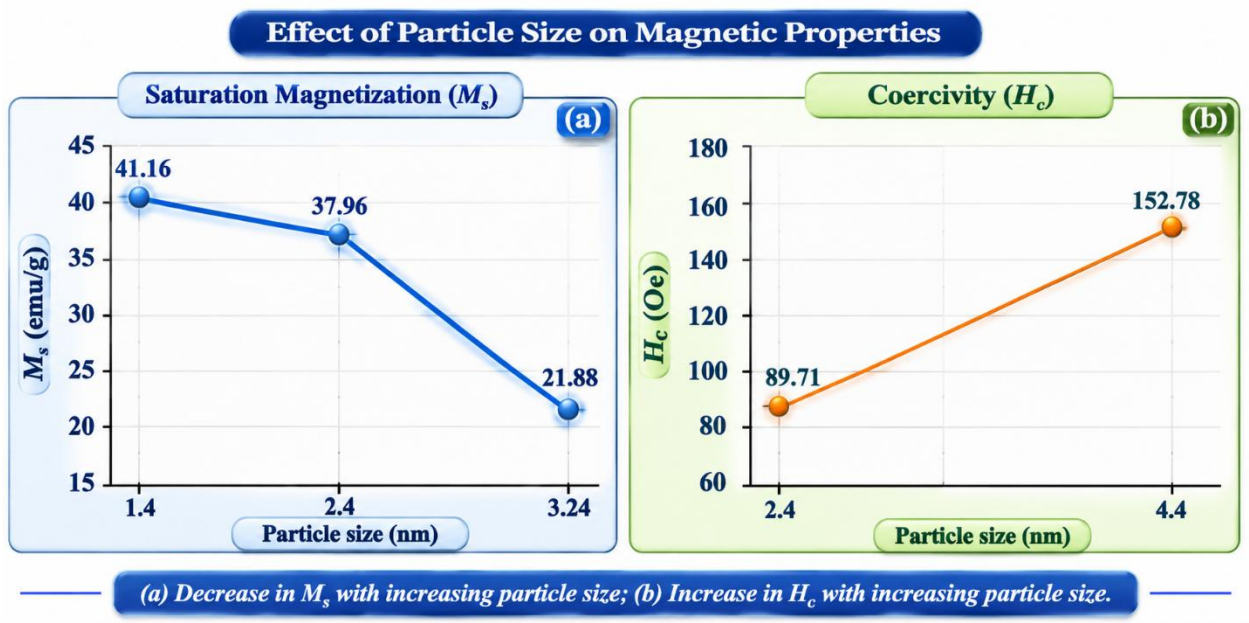

Figure 9. Saturation magnetization and coercivity of NixFe3−xO4 versus Ni:Fe ratio. Only the values reported in the text of [1] are plotted; the other ratios were not reported.

Table 8 and Figure 9 show that composition alone changes the magnetic response of $NixFe_{3-x}O_4$: the saturation magnetization decreased from 40.16 emu/g at Ni:Fe = 1:4 to 37.96 emu/g at 2:4

and to 21.97 emu/g at higher ratios, while the coercivity increased from 89.71 to 153.09 Oe and Ms/Mr decreased from 7.05 to 3.77. A lower Ms and a higher Hc make the material magnetically harder, which is less favorable for low-loss soft cores and connects this nanoparticle result with the hysteresis-loss discussion in Section 5.7. The source text reports only these values, so intermediate ratios are not plotted.

5.2 Coercivity

Coercivity (Hc) is the reverse magnetic field required to reduce the magnetization of a material to zero after saturation. It quantifies the resistance to magnetization reversal and is closely related to magnetic anisotropy and domain wall motion. For power electronic applications, low coercivity is generally preferred because it minimizes hysteresis losses during repeated cycles of magnetization. Ferrites exhibiting soft magnetic behavior require less energy for magnetization reversal, thereby improving the conversion efficiency [3–5]. For example, the coercive field is 5–15 A/m in Mn–Zn ferrites and 200–300 A/m in Ni–Zn ferrites [3]. Coercivity depends on factors such as particle size, magnetocrystalline anisotropy (MCA), grain boundaries, internal stress, defect concentration, and dopant species concentration. The relationship between coercivity and anisotropy is approximated by $Hc \approx 2K1/\mu_0 Ms$, where K1 is the magnetocrystalline anisotropy constant and μ0 is the permeability of free space (the Stoner–Wohlfarth coherent-rotation limit). Mn–Zn and Ni–Zn ferrites follow this trend: an anisotropy constant of 10–100 J/m³ goes with a coercive field of 5–15 A/m, and one of up to a few kJ/m³ with 200–300 A/m [3]. Mg–Zn and Ni–Zn ferrites typically exhibit relatively low coercivity and are therefore widely employed in high-frequency magnetic core applications [4, 5]. In contrast, $CoFe_2O_4$ possesses significantly higher coercivity owing to its large anisotropy, making it more suitable for permanent magnetic or spintronic applications than for low-loss power electronics [45, 108–112].

5.3 Remanent Magnetization

Remanent magnetization (Mr) is the residual magnetization that remains after the removal of an external magnetic field[113]. High remanence is advantageous for permanent magnets and magnetic memory devices; however, power electronics generally require low remanence to reduce the residual magnetic flux and minimize hysteresis losses during rapid switching [4, 5]. The squareness ratio, defined as S = Mr/Ms, provides insight into the magnetic domain structure, where low squareness values typically indicate multidomain behavior and soft magnetic

characteristics that are desirable for high-frequency inductive components [1, 5]. In the $Ni_xFe_{3-x}O_4$ samples of Table 8, the Ms/Mr ratio fell from 7.05 to 3.77, which corresponds to a squareness S = Mr/Ms rising from about 0.14 to 0.27 (derived from the reported ratios); this rise accompanied the increase of the coercivity from 89.71 to 153.09 Oe, so the Ni-rich sample is both harder and more square [1]. Techniques such as thermal annealing, particle size optimization, and cation redistribution can effectively tune the remanence while maintaining an adequate saturation magnetization [1, 2].

5.4 Initial Magnetic Permeability

The initial permeability (μi) characterizes the ease of magnetic flux establishment within a material under small applied magnetic fields, with high permeability enabling efficient flux concentration and reducing the number of coil turns required in inductors and transformers. Permeability depends on factors such as saturation magnetization, grain size, domain wall mobility, porosity, and magnetic anisotropy, with larger grains, fewer defects, and improved crystallinity generally resulting in higher permeabilities[114]. This property is increasingly important as power converters shift toward switching frequencies above several megahertz, where ferrite materials with optimized permeability facilitate the miniaturization of passive magnetic components without compromising their efficiency.

Table 9 shows how the sintering schedule changes the microstructure and conductivity of a Mn–Zn ferrite: the average grain size increased from 11.4 to 19.8 μm and the 10 MHz conductivity varied between 56.8 and 82 Ω^{-1} m^{-1}, while the initial permeability decreased because the effective anisotropy rose from about 50 to about 67 J/m^3 [3].

Table 9. Physical parameters of Mn–Zn ferrite rings (70 wt% Fe_2O_3, 24 wt% MnO, 6 wt% ZnO with NbO_2 and CaO) sintered under different schedules. Data from [3].

Sample	Sintering T (°C)	Sintering time (h)	Density (kg/m³)	Grain size (μm)	σDC (Ω^{-1} m^{-1})	σ at 10 MHz (Ω^{-1} m^{-1})	Js (T)
A	1325	3	4830	11.4	0.146	56.8	0.55
D	1340	3	4850	12.3	0.214	82	0.55
G	1360	3	4900	15.1	0.220	80	0.55
I	1360	7	4890	19.8	0.215	71	0.55

Table 9 adds density and saturation polarization to the microstructure shown in Figure 7: the density rose only from 4830 to 4900 kg/m^3 and Js stayed at 0.55 T, so the loss increase of about 40% between samples A and I (at 100 kHz and 100 mT) is accompanied by larger grains and a

higher effective anisotropy (about 50 to 67 J/m³ after sintering at 1360 °C), not by lower density or lower magnetization. The higher anisotropy also goes with a lower initial permeability, which links this table to Section 5.4.

5.5 Curie Temperature

The Curie temperature (TC) marks the transition between ferromagnetic (or ferrimagnetic) and paramagnetic behaviors, with long-range magnetic ordering present below TC and thermal fluctuations disrupting spin alignment above it, leading to a significant reduction in magnetization. For reliable operation, ferrites must maintain stable magnetic properties across the expected operating-temperature range, where elevated Curie temperatures enhance thermal stability, particularly in processors and data center electronics that may experience localized temperatures exceeding 100 °C. Enhancements such as rare-earth substitution, optimized cation distribution, and improved crystallinity have been demonstrated to improve thermal stability without substantially compromising soft magnetic behavior[115, 116].

5.6 Magnetic Anisotropy

Magnetic anisotropy describes the direction-dependent magnetization originating from crystallographic symmetry, particle morphology, strain, and spin–orbit coupling. Moderate anisotropy is desirable because it balances magnetic stability with low coercivity. Excessive anisotropy increases the hysteresis losses, whereas insufficient anisotropy reduces the magnetic stability. Common methods for controlling anisotropy include rare-earth doping, shape engineering, stress engineering, core–shell nanostructures, and surface functionalization. Optimizing anisotropy enhances both the magnetic performance and thermal reliability of electronic hardware systems[117–119].

5.7 Magnetic Loss Mechanisms

Magnetic losses determine the energy efficiency of ferrite components that operate under alternating magnetic fields. The total magnetic loss can be conceptually expressed as the sum of the hysteresis, eddy current, and residual or anomalous losses, as represented by equation ($P_{total} = P_h + P_e + P_r$). Hysteresis loss results from repeated magnetization reversals and is proportional to the area enclosed by the hysteresis loop. Minimizing the hysteresis loss involves reducing both coercivity and remanence, which directly decreases the energy dissipated during

each magnetization cycle[120, 121].Eddy-current losses arise from induced circulating currents generated during alternating magnetic fields. Owing to the high electrical resistivity of ferrites, eddy current losses are significantly lower than those of metallic magnetic materials. This property is a key advantage of power electronics operating at high frequencies[122–125]. Residual losses encompass contributions from spin relaxation, domain wall resonance, defects, and microstructural heterogeneities in the material. These losses become increasingly significant in the MHz–GHz frequency range, which is particularly relevant to modern electronic systems[3, 123, 126–128].

Table 10 compares commercial Mn–Zn and Ni–Zn ferrites quantitatively.

Table 10. Quantitative comparison of commercial-grade Mn–Zn and Ni–Zn soft ferrites. Data from [3]; commercial grades: EPCOS N87 and T38 (Mn–Zn), Ferroxcube 4C65 (Ni–Zn).

Property	Mn–Zn ferrite	Ni–Zn ferrite
DC resistivity	A few Ω m (N87: 6.3 Ω m; T38: 8.5 × 10^{-2} Ω m); falls by more than one order of magnitude at MHz	> 10^{5} Ω m
DC conductivity	≈ 0.1–1 Ω^{-1} m^{-1}	≈ 10^{-5} Ω^{-1} m^{-1} (4C65)
Anisotropy constant K (20–120 °C)	≈ 10–100 J/m^3	Up to a few kJ/m^3
Coercive field	5–15 A/m	200–300 A/m
Average grain size	≈ 10–20 µm (studied samples 10.8–19.8 µm)	≈ 1–2 µm
Permeability response	Real permeability peaks at a few hundred kHz	Cutoff about one order of magnitude higher; peak ≈ 15 MHz (4C65)
Eddy-current losses	Relevant above ≈ 6–10 MHz in 5 mm rings; from ≈ 10 kHz in the low-resistivity T38 grade	Negligible
Loss versus frequency	Lower at low frequency	> 10× higher at low frequency; lower than Mn–Zn above ≈ 1 MHz
Activation energy of key relaxation	0.21 eV (grain-boundary conduction)	0.66 eV (diffusion aftereffect, τ ≈ 0.1 s)

Figure 10 plots the same quantities on logarithmic axes and shows that the two families differ by orders of magnitude in resistivity, coercivity, and anisotropy.

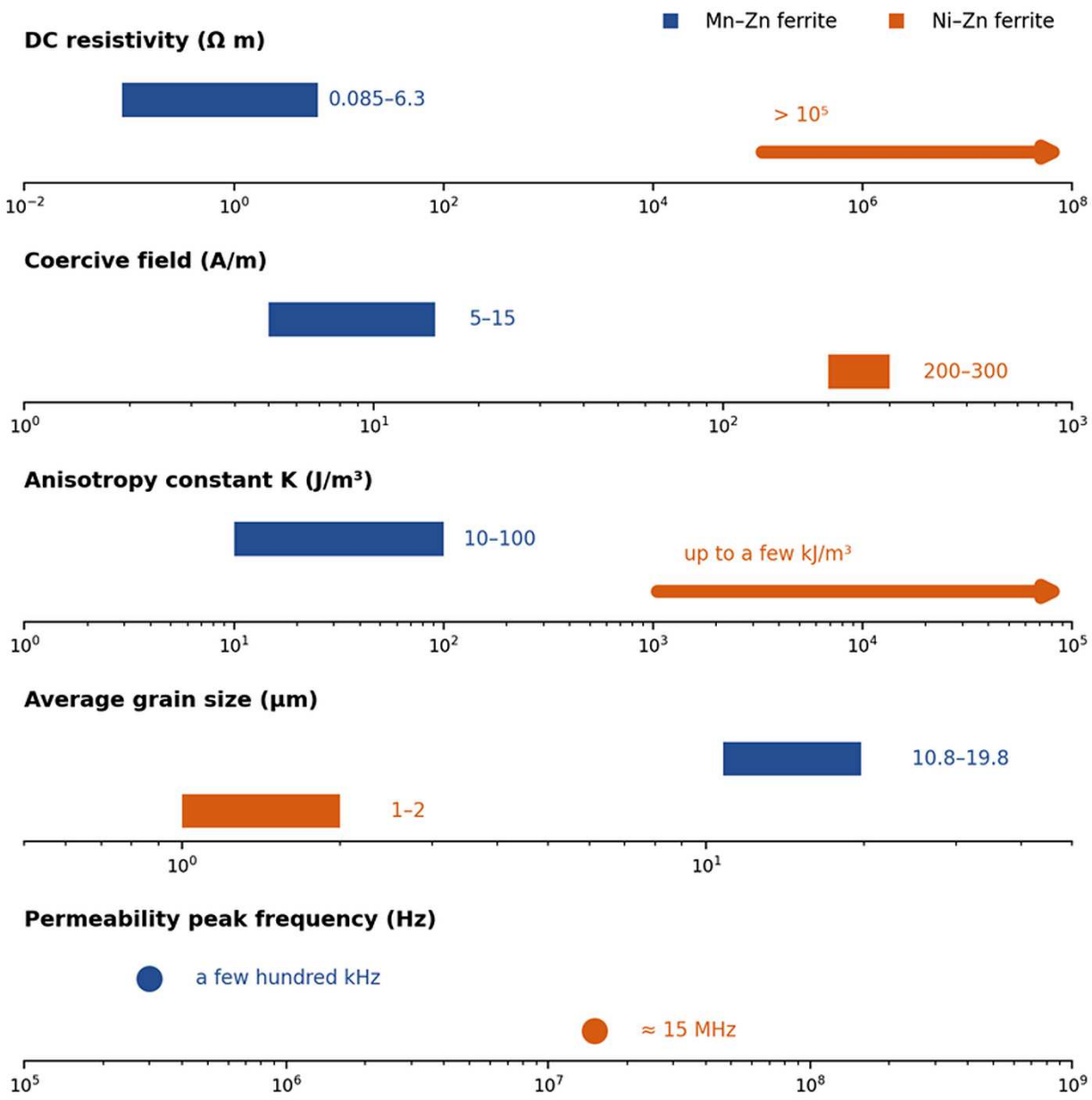

Figure 10. Mn–Zn versus Ni–Zn ferrites: resistivity, coercive field, anisotropy constant, grain size, and permeability peak frequency (log scales). Values from [3]. Arrows mark values reported only as lower bounds (Ni–Zn resistivity > 10^5 Ω m; anisotropy up to a few kJ/m³).

Table 10 and Figure 10 show that Mn–Zn and Ni–Zn ferrites differ by orders of magnitude in every parameter that controls loss: resistivity (0.085–6.3 versus above 10^5 Ω m), coercive field (5–15 versus 200–300 A/m), anisotropy (10–100 J/m³ versus up to a few kJ/m³), grain size (10.8–19.8 versus 1–2 µm), and permeability peak frequency (a few hundred kHz versus about

15 MHz). The low resistivity explains why eddy-current loss limits Mn–Zn ferrites at MHz frequencies, whereas the high coercivity and anisotropy explain the higher low-frequency loss of Ni–Zn; both effects enter the loss components of Table 11 and the selection guide of Table 13.

Table 11 separates the loss components and gives the frequency ranges in which each dominates.

Table 11. Loss components of soft ferrites with reported frequency ranges and numbers. Data from [3].

Component	Origin	Reported behavior	Material notes
Hysteresis loss (Wh)	Irreversible domain-wall displacements (Barkhausen jumps)	Quasi-static; scales as Jp^2.8; disappears as walls relax around 1–2 MHz	Separated in Mn–Zn by extrapolating W(f) to f → 0
Classical eddy-current loss	Macroscopic eddy-current paths	Above ≈ 6 MHz in 5.02 mm Mn–Zn rings; skin depth ≈ 2 mm at 1 GHz; from ≈ 10 kHz in the low-resistivity T38 grade	Negligible in Ni–Zn
Excess loss by spin damping (Wexc,sd)	Friction on moving domain walls	Wexc,sd ∝ f^n with n ≈ 0.9 (n = 0.5 in soft magnetic sheets)	Vanishes as walls relax in the MHz range
Rotational loss (Wrot,sd)	Resonant spin precession (Landau–Lifshitz)	Accounts for the loss from ≈ 800 kHz (Jp = 2 mT) and ≈ 3–5 MHz (Jp = 200 mT) in thinned Mn–Zn rings	Shifts above ≈ 10 MHz in Ni–Zn
Diffusion aftereffect (Waf)	Cation diffusion hindering wall motion	Time constant ≈ 0.1 s at room temperature; activation energy 0.66 eV	Ni–Zn only

Table 11 assigns each loss component to a frequency range: hysteresis and excess loss dominate below about 1–2 MHz, rotational loss starts near 0.8 MHz at 2 mT and at 3–5 MHz at 200 mT, and eddy-current loss appears above about 6 MHz in a 5 mm Mn–Zn ring or from about 10 kHz in the low-resistivity T38 grade. The resistivity values of Table 10 therefore decide where each material leaves the low-loss regime, and these ranges are mapped in Figure 11.

5.8 Frequency-Dependent Magnetic Behavior

As the switching frequency increases, the magnetic permeability of ferrite materials generally decreases owing to relaxation processes and domain wall dynamics. To extend the useful frequency range, researchers have developed several strategies, including nanocrystalline microstructures, reduced grain sizes, high-resistivity compositions, rare-earth substitutions, composite magnetic materials, and thin-film ferrites[129–131].

5.9 Dopant Engineering

Chemical substitution through dopant engineering is a critical strategy for tailoring the magnetic properties of spinel ferrites to meet specific application requirements, as summarized in table.3.

The table summarizes how various dopants influence key magnetic characteristics such as coercivity, saturation magnetization, permeability, anisotropy, and thermal stability.

For instance, Mg^{2+} reduces coercivity, making it suitable for high-frequency inductors, while Mn^{2+} enhances saturation magnetization[132], which benefits power transformers. Similarly, Zn^{2+} improves permeability important for voltage regulators, and Co^{2+} increases anisotropy, a property leveraged in spintronic devices[133–135]. Dopants such as Cu^{2+} modify electrical transport, aiding integrated electronics, whereas Gd^{3+} enhances thermal stability, which is crucial for processors operating under high thermal loads[136, 137]. Rare-earth dopants such as La^{3+}, Nd^{3+}, and Y^{3+} further refine grain size, improve magnetic ordering, and reduce magnetic loss, respectively, thus optimizing performance in embedded magnetic components, magnetic memory, and EMI suppression. By combining multiple dopants, researchers can finely tune ferrite compositions to achieve a balanced combination of magnetic performance, thermal resilience, and electrical properties tailored to specific technological demands[138–140].

5.10 Relationship Between Magnetic Properties and Device Performance

The reviewed studies consistently demonstrate that magnetic optimization directly influences the efficiency of electronic hardware by enabling a higher saturation magnetization, which allows for greater magnetic energy storage and reduces the volume of inductive components[141–145]. Ferrite systems can be engineered for high-frequency operation extending from the MHz regime toward higher frequencies, although permeability dispersion, ferromagnetic resonance, relaxation losses, and processing-dependent losses constrain the practical operating window[129, 146, 147]. Enhanced permeability contributes to better voltage regulation and transient response, and elevated Curie temperatures ensure reliable operation under high thermal loads[148, 149]. Magnetic property optimization is the foundation for the successful integration of ferrite nanoparticles into power electronics. Through composition engineering, cation redistribution, defect modulation, morphology control, and advanced synthesis techniques, ferrites can be tailored to achieve a combination of high saturation magnetization, low coercivity, high permeability, thermal stability, and minimal magnetic losses required for next-generation electronic systems.

6. Ferrite Nanoparticles in Power Delivery and EMI Suppression

6.1 Applications in Power Delivery Networks

Ferrite magnetic nanoparticles are used in integrated inductors, high-frequency transformers, voltage regulator modules, DC–DC converters, embedded magnetic components, and EMI suppression elements. Matching the ferrite system to the operating frequency, flux density, and temperature determines the efficiency and stability of these power systems (Table 12).

6.2 Comparison of Ferrite Systems for Power Electronics

$MgFe_2O_4$ ferrites exhibit low coercivity and moderate saturation magnetization, which translates to low hysteresis losses and excellent thermal stability. Their stable behavior under thermal stress ensures reliable operation in demanding power delivery environments[150–152].

Table 12. Comparative assessment of ferrite systems for power-electronics applications. References per system are those of Table 3.

Ferrite system	Key magnetic characteristics	Principal advantages	Representative applications	Reference
$MgFe_2O_4$	Low coercivity, moderate saturation magnetization	Low hysteresis losses, excellent thermal stability	High-frequency inductors, voltage regulator modules	[31, 32]
$NiFe_2O_4$	High permeability, good frequency stability	Efficient magnetic flux concentration	Integrated inductors, DC–DC converters	[33]
$MnFe_2O_4$	High saturation magnetization	High magnetic energy density	Wireless power transfer, transformer cores	[39]
$ZnFe_2O_4$	High electrical resistivity	Reduced eddy-current losses	EMI suppression, filtering components	[34–37]
Mg–Zn ferrites	Low magnetic losses	Stable high-frequency operation	Processor power delivery networks	[43]
Ni–Zn ferrites	Excellent soft magnetic behavior	Compact magnetic components	Embedded inductors, high-frequency converters	[44–47]
Mn–Zn ferrites	High permeability and flux density	Efficient power conversion	Server power supplies, data-center transformers	[48–51]
$CoFe_2O_4$	High anisotropy and coercivity	Strong magnetic stability	Magnetic sensors	[38]
Rare-earth-doped ferrites	Enhanced thermal stability and tailored magnetic properties	Improved reliability under demanding operating conditions	Advanced processors, heterogeneous chip packages	[52–55]

Table 12 translates the parameters into component choices: Mg and Mg–Zn ferrites (low coercivity, low loss) for inductors and voltage regulator modules, Ni and Ni–Zn ferrites (high permeability, high-frequency operation) for converters and embedded inductors, Mn and Mn–Zn ferrites (high saturation magnetization and permeability) for transformers and power supplies,

and $ZnFe_2O_4$ (high resistivity) for EMI filtering. These assignments follow the benchmark values of Table 10 and the frequency limits of Table 13.

$NiFe_2O_4$ ferrites are characterized by high permeability and good frequency stability, enabling efficient magnetic flux concentration. This makes them ideal for integrated inductors and DC–DC converters, which require precise magnetic control to achieve efficient voltage regulation and power conversion. The frequency stability of $NiFe_2O_4$ enhances performance consistency across varying operational conditions typical in electronic systems[153–157]. $MnFe_2O_4$ and $ZnFe_2O_4$ ferrites serve specialized roles owing to their unique magnetic properties. $MnFe_2O_4$, with its high saturation magnetization and magnetic energy density, is well-suited for wireless power transfer and transformer cores, where strong magnetic fields and energy efficiency are essential requirements. Conversely, $ZnFe_2O_4$ offers high electrical resistivity, which reduces eddy-current losses, making it effective for EMI suppression and filtering components, critical for maintaining signal integrity in sensitive electronic systems[110, 158–162]. Advanced ferrite systems such as Mg–Zn, Ni–Zn, Mn–Zn, $CoFe_2O_4$, and rare-earth-doped ferrites provide tailored solutions for specific electronic hardware challenges. Mg–Zn ferrites deliver low magnetic losses and stable high-frequency operation, supporting processor power delivery networks[45, 111, 163]. Ni–Zn ferrites combine excellent soft magnetic behavior with compactness, benefiting embedded inductors and high-frequency converters[45, 164–167]. Mn–Zn ferrites offer high permeability and flux density, optimizing power conversion in server supplies and data-center transformers[168]. $CoFe_2O_4$ ferrites, with high anisotropy and coercivity, provide strong magnetic stability for spintronic devices and sensors[169], while rare-earth doping enhances thermal stability and magnetic properties, improving reliability in advanced processors and heterogeneous chip packages[137, 170–174]. The comparative analysis highlighted that no single ferrite composition is universally optimal. Instead, the selection depends on the specific balance required between the saturation magnetization, permeability, coercivity, frequency response, and thermal stability. Therefore, composition engineering and controlled microstructural design play pivotal roles in tailoring ferrite nanoparticles for diverse power delivery applications. The reviewed studies collectively demonstrate that ferrite magnetic nanoparticles represent a versatile platform for improving power delivery in sustainable electronics applications. Continued

advances in composition engineering, thin-film processing, and semiconductor integration are expected to further expand their role in integrated power delivery networks, contributing to reduced energy consumption and improved hardware reliability.

6.3 EMI Suppression and Electromagnetic Compatibility

High-speed switching in power delivery networks generates electromagnetic interference that degrades signal integrity and raises error rates (Section 1.2). Ferrites are suited to suppressing this interference because their high electrical resistivity limits eddy-current losses while frequency-dependent permeability losses attenuate unwanted high-frequency currents [175–182]. The loss mechanisms that are penalized in a power inductor, namely permeability dispersion, ferromagnetic resonance, and relaxation, can therefore be exploited deliberately in suppression beads, filters, and shielding structures. This means that the same composition cannot be evaluated against a single criterion: a ferrite optimized for low loss at the converter switching frequency (Section 5.7 and 5.8) is not necessarily the best choice for broadband attenuation. Few of the reviewed studies quantify electromagnetic compatibility performance against electronic-hardware metrics, which is the gap identified in Section 1.5.

6.4 Frequency-Based Selection Guide

Combining the benchmarks above gives a practical frequency-based guide (Table 13). Figure 11 maps the frequency ranges in which each loss mechanism is reported to matter and the frequency at which the lower-loss family changes. The guide is derived solely from the cited numbers and applies to the compared grades; extending it to other compositions requires data measured under the same conditions (Section 9.2).

Table 13. Frequency-based selection guide for Mn–Zn and Ni–Zn ferrites, derived from the numbers reported in [3] for the commercial grades N87, T38 (Mn–Zn) and 4C65 (Ni–Zn). Thresholds depend on grade, core size, and drive level.

Frequency range	Dominant loss mechanisms reported	Lower-loss family for the compared grades	Basis
< 1 MHz	Domain-wall hysteresis and excess loss; eddy currents already relevant in low-resistivity Mn–Zn (T38 from ≈ 10 kHz)	Mn–Zn (N87)	Ni–Zn 4C65 loss > 10× higher at low frequency [3]
≈ 1 MHz	Domain walls relax (1–2 MHz); rotational loss starts (≈ 0.8 MHz at 2 mT)	Crossover	Ni–Zn loss persistently lower above ≈ 1 MHz [3]
≈ 1–10 MHz	Rotational loss (3–5 MHz at 200 mT); eddy-current loss	Ni–Zn	Mn–Zn resistivity falls > 10×; Ni–Zn > 10^5 Ω m [3]

	grows in Mn–Zn rings (> 6 MHz in a 5 mm ring)		
≥ 10 MHz up to ≈ 1 GHz	Spin precession; Ni–Zn permeability peak near 15 MHz; skin depth ≈ 2 mm at 1 GHz	Ni–Zn	Preferred where frequencies reach or exceed 10 MHz [3]
Temperature window	Mn–Zn loss minimum at 80–100 °C; flattest permeability and loss with 3000–4000 ppm CoO between −20 and 130 °C	Mn–Zn with CoO	[3]

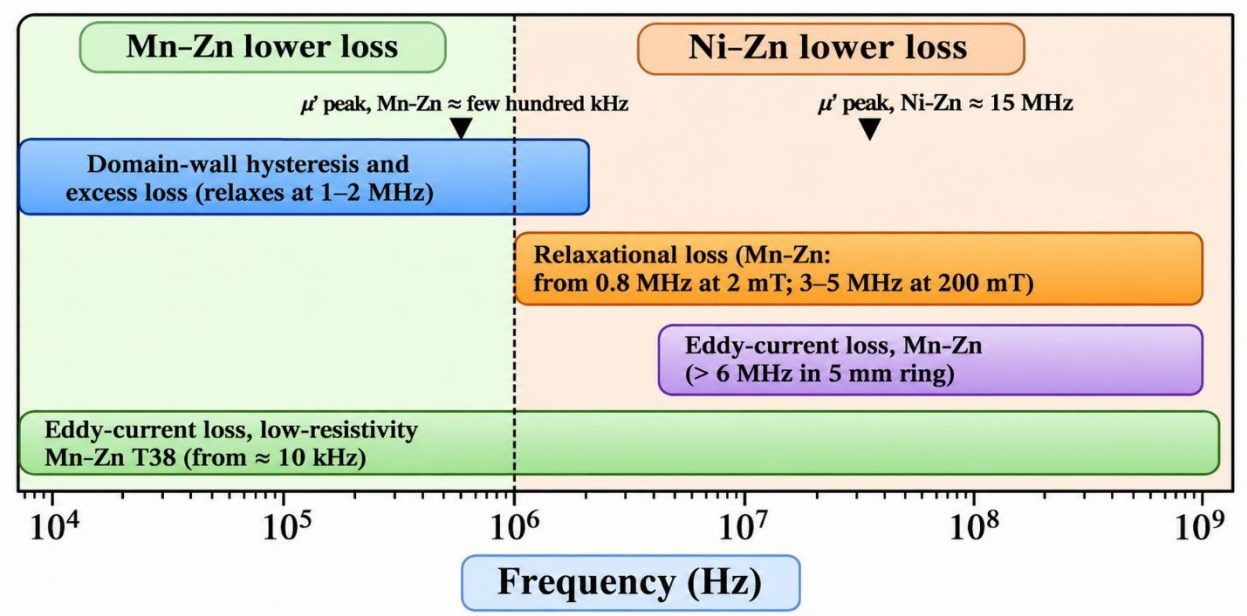

Figure 11. Frequency map of loss mechanisms and of the lower-loss ferrite family for the compared Mn–Zn (N87, T38) and Ni–Zn (4C65) grades. Derived from the values reported in [3].

Table 13 and Figure 11 combine the benchmarks into one guide: below about 1 MHz the Mn–Zn grade N87 has the lower loss, near 1 MHz the two families cross, and above about 1 MHz the Ni–Zn grade 4C65 has the lower loss and is preferred from about 10 MHz. Within the Mn–Zn range, operating near the loss minimum at 80–100 °C and using 3000–4000 ppm CoO keeps permeability and loss stable between −20 and 130 °C. These statements are derived from the numbers of Dobák et al. and are limited to the compared grades.

7. Thermal Management and Solid-State Cooling

7.1 Thermal Requirements and Evaluation Metrics

Localized hotspots degrade the performance and reliability of compact electronic and power devices (Section 1.4). Ferrite nanoparticles contribute to several complementary thermal strategies [7–13]. Meaningful comparison of these strategies requires common metrics: thermal conductivity or its enhancement relative to the matrix, interfacial thermal resistance, hotspot temperature under a defined heat flux, retention of electrical insulation, and stability under thermal cycling. Most of the reviewed studies report only the first of these, and comparatively few report chip-level or module-level thermal resistance.

7.2 Ferrite-Filled Thermal Interface Materials and Phase-Change Composites

Ferrite nanoparticles dispersed in polymer matrices raise thermal conductivity while preserving electrical insulation [87–93]. A quantitative example is Fe_3O_4 in low-density polyethylene: at 7 vol% the thermal conductivity reached 0.384 W/(m K), which is 21.88% above the matrix (0.315 W/(m K)), and 0.461 W/(m K), 46.27% above the matrix, when the particles were aligned into chains by a 1.0 T field during processing [183]. The gain from alignment shows that filler arrangement matters as much as filler content. The practical limits are the trade-off between filler loading and the processability and mechanical behavior of the composite, the quality of filler dispersion, and the interfacial resistance between filler and matrix. Phase-change composites buffer transient heat loads but do not provide continuous heat removal; ferrite-specific numbers for them were not available in the sources reviewed here.

7.3 Magnetic Nanofluids and Thermoelectric Heat Distribution

Magnetic nanofluids containing ferrite nanoparticles show enhanced thermal transport under an applied magnetic field [94–97]. In a water-based Fe_3O_4 ferrofluid with 5.0 vol% of 10 nm particles, the thermal conductivity rose by more than 200% at its maximum under a field, whereas no enhancement was observed without a field [184]. The field dependence is both the main advantage and the main constraint: a field source is required, and the conductivity does not return immediately to its starting value when the field is removed [184]. Colloidal stability and the leakage and sealing risks of liquid cooling remain open issues. For thermoelectric architectures, system-level demonstrations at application-relevant heat fluxes are scarce.

7.4 Magnetocaloric Ferrites

Certain ferrites exhibit the magnetocaloric effect, in which a magnetic entropy change produces reversible heating and cooling under an applied field, offering refrigeration without greenhouse gases [81–86]. Reported values for ferrite nanomaterials are modest and appear at low temperature: $CoFe_2O_4$ nanofibers showed a maximum entropy change of 1.71 J/(kg K) near 32 K, an adiabatic temperature change of 0.93 K at 180 K, and a relative cooling power of 7.58 J/kg at 35 kOe [185]. Whether such values can be reached near room temperature, with fast heat-transfer kinetics, cycling stability, and a practical field source, has been demonstrated far less often than material-level characterization.

7.5 Comparative Assessment of Thermal-Management Pathways

Table 14 compares the thermal-management pathways.

Table 14. Thermal-management pathways in which ferrite nanoparticles contribute, with reported advantages and open limitations.

Pathway	Role of ferrite nanoparticles	Reported advantage	Open limitation	Reported quantitative result
Polymer thermal interface materials [14–20]	Filler that raises thermal conductivity	Improved heat transfer between heat source and heat spreader with retained electrical insulation	Filler loading versus processability; interfacial resistance; dispersion quality	Fe_3O_4/LDPE, 7 vol%: 0.384 W/(m K), +21.88%; 0.461 W/(m K), +46.27% with field-aligned chains [183]
Phase-change composites [14–20]	Additive that improves conduction in the storage medium	Improved thermal conductivity, mechanical stability, and cycling durability	Buffers transient loads only; no continuous heat removal	Not quantified in the sources reviewed here
Magnetic nanofluids [21–24]	Dispersed particles responsive to a magnetic field	Field-responsive, adaptive heat transport	Colloidal stability; field source; leakage and sealing risks	Fe_3O_4/water, 5.0 vol%, 10 nm: > +200% under a field, none without [184]
Thermoelectric modules [21–24]	Heat-distribution enhancement in the module	Improved heat spreading in integrated cooling modules	Few system-level demonstrations at application-relevant heat fluxes	Not quantified in the sources reviewed here
Magnetocaloric refrigeration [25–30]	Active magnetocaloric material	Solid-state cooling without greenhouse gases	Temperature change, heat-transfer kinetics, cycling stability, integration	$CoFe_2O_4$ nanofibers: $\|\Delta S\|$ = 1.71 J/(kg K) near 32 K; ΔT_{ad} = 0.93 K at 180 K; RCP 7.58 J/kg at 35 kOe [185]

Figure 12 compares the reported enhancements of thermal conductivity.

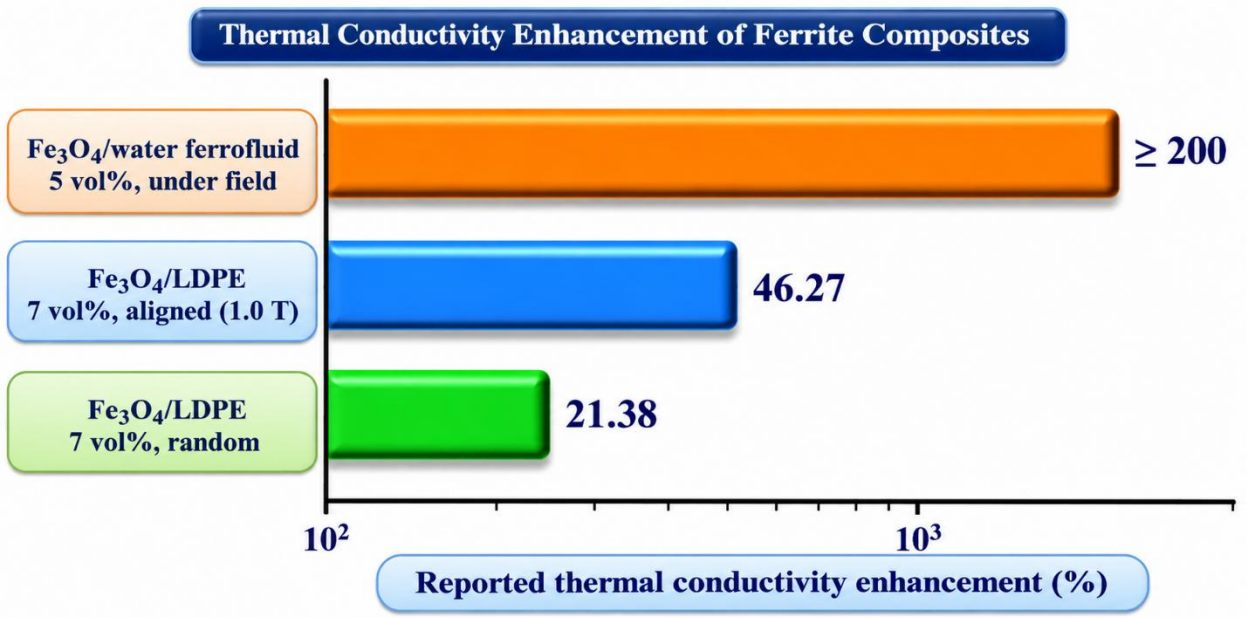

Figure 12. Reported thermal conductivity enhancement of Fe_3O_4-based composites and ferrofluids relative to the polymer matrix or base fluid. Data from [183] and [184]; the ferrofluid value is a lower bound (more than 200% at maximum). Magnetocaloric performance is not included because it is not measured on the same metric.

Table 14 and Figure 12 show that the pathways differ in kind, not only in size. The thermal conductivity of Fe_3O_4/LDPE rose by 21.88% for random filler and by 46.27% when the particles were aligned in a 1.0 T field, so filler arrangement matters as much as loading. The ferrofluid gained more than 200% but only under a field, so it needs a field source, and the magnetocaloric example (1.71 J/(kg K) near 32 K) lies far from room temperature. Pathways without verified numbers are marked as such, and Table 15 lists the thermal metrics that future studies should report.

8. Sustainability and Lifecycle Considerations

Finally, sustainability should be evaluated across the entire material lifecycle, including raw material availability, synthesis energy, solvent and precursor consumption, processing temperature, device lifetime, recyclability, and end-of-life management. Therefore, a ferrite material should be considered sustainable only when its improvements in power efficiency, thermal management, reliability, or component miniaturization outweigh the environmental and economic costs associated with its synthesis and integration. Quantitative lifecycle evidence, for example synthesis energy and solvent use of the main routes (co-precipitation, sol–gel,

hydrothermal, combustion, green synthesis), the critical-raw-material content of Co- and Ni-containing compositions, and recyclability or end-of-life data, with references.

9. Challenges and Future Research Directions

9.1 Materials-to-Device Translation and Manufacturing

Most investigations concentrate on material-level characterization of isolated properties, while comparatively few establish direct relationships between ferrite composition and application-level metrics such as power-conversion efficiency, high-frequency loss density, electromagnetic compatibility, and thermal resistance. Standardized testing protocols are also lacking: because the loss ranking of Mn–Zn and Ni–Zn ferrites reverses near 1 MHz [3], results measured at different frequency, peak polarization, or core thickness cannot be compared directly.

Manufacturing is a second barrier. Routes that give narrow size distributions (co-precipitation, solvothermal, microwave-assisted) operate at roughly 60–200 °C but need calcination at about 500–600 °C for crystallinity [2], whereas the dense polycrystalline cores of commercial power magnetics are sintered at about 1325–1360 °C [3]. Translating nanoparticle properties into dense, low-loss cores without excessive grain growth, and into thin films compatible with semiconductor processing, remains an open challenge. Agglomeration, broad size distributions, limited reproducibility, and long-term chemical and thermal stability further restrict practical use [1].

9.2 Future Research Directions

Table 15 lists the research priorities and the minimum data that future studies should report so that results become comparable and device-relevant.

Table 15. Research priorities and the minimum data that studies should report. Loss-measurement practice follows [3]; nanoparticle characterization follows [1].

Priority	Gap identified	Minimum data to report
Standardized loss benchmarking	Loss ranking reverses with frequency (Ni–Zn versus Mn–Zn)	Energy loss and complex permeability at stated peak polarization (for example 2, 10, 50, 100 mT), frequency, temperature, core thickness, and resistivity
Temperature-stable compositions	Loss minimum at 80–100 °C; permeability and loss drift with temperature	Permeability and loss from −20 to 130 °C; additive level (for example CoO in ppm)
Nanoparticle-to-core translation	Size, strain, and cation distribution change Ms, Hc, and Mr	Size (XRD and SEM), cation distribution, Ms, Hc, Mr, and processing temperature and time

Quantified thermal pathways	Thermal conductivity, interfacial resistance, and adiabatic temperature change rarely reported	Conductivity enhancement versus filler fraction, interfacial thermal resistance, adiabatic temperature change
Scalable low-temperature synthesis	Routes above 800 °C are energy-intensive	Peak temperature, time, yield, and phase purity per route
Lifecycle and sustainability	Little energy and raw-material data	Synthesis energy, critical-element content, and recyclability
Data-driven design	Machine-learning models need consistent datasets	Standardized property tables with measurement conditions

Table 15 turns the gaps found in Sections 5 to 7 into reporting requirements: loss at a stated polarization, frequency, temperature, and core thickness (from Table 11), temperature range and additive level (from Table 6), size, cation distribution, and processing data (from Table 7 and Table 2), and thermal metrics (from Table 14). Adopting these requirements would make the benchmarks in this review directly comparable across studies.

Data-driven approaches, including machine-learning models trained on standardized datasets, can accelerate the exploration of composition–structure–property relationships and identify compositions that satisfy magnetic, electrical, thermal, reliability, and sustainability constraints at the same time [1]. Multifunctional nanocomposites, thin-film integration, and chip-scale thermal solutions should be developed together with lifecycle assessment so that gains in efficiency are not offset by the energy and raw-material cost of fabrication.

10. Conclusions

This critical review links composition, cation distribution, and microstructure to the magnetic, electrical, and thermal performance of spinel ferrite nanoparticles for high-frequency power magnetics, EMI suppression, and thermal management.

The quantitative evidence shows that no single ferrite is optimal. Mn–Zn ferrites offer high permeability but a resistivity of only a few Ω m, whereas Ni–Zn ferrites exceed 10^5 Ω m and extend useful permeability to about 10–15 MHz at the cost of a coercive field of 200–300 A/m [3]. Processing is as important as composition: a longer and hotter sintering schedule raised the grain size from 11.4 to 19.8 μm and the loss at 100 kHz by about 40%, and 3000–4000 ppm CoO flattened the temperature dependence [3].

At the nanoscale, composition changes the magnetic response markedly, for example the saturation magnetization of NixFe3−xO4 fell from 40.16 to 21.97 emu/g while the coercivity rose from 89.71 to 153.09 Oe [1], and the synthesis route sets the temperature budget from 60–200 °C for wet-chemical routes to more than 800 °C for solid-state routes [1, 2].

Ferrite-filled thermal interface materials, phase-change composites, magnetic nanofluids, and magnetocaloric ferrites offer complementary pathways to heat management, but their effectiveness depends on conductivity enhancement, interfacial resistance, temperature change, and cycling stability, which are rarely quantified.

Tunable ferrite nanoparticles are therefore a promising materials platform rather than a universally validated solution. Standardized loss benchmarking, temperature-stable compositions, scalable low-temperature fabrication, quantified thermal metrics, lifecycle assessment, and data-driven design are the priorities for moving from material-level results to device-level performance.

Declarations

Funding: The authors received no specific funding for this work.

Data availability: Not applicable.

Ethics approval and consent to participate: Not applicable.

Consent for publication: Not applicable.

Competing interests: The authors declare no competing interests.

Third-party material: Not applicable.

Acknowledgements

The authors sincerely thank the PG & Research Department of Physics at St. Joseph's College of Arts and Science (Autonomous), Cuddalore-607001, affiliated with Annamalai University, India, for providing the essential library resources.

References

1. Mataev M, Madiyarova A, Abdraimova M, Tursyn Z, Ramachandran K (2026) Structure Property–Application Relationships of Spinel Ferrite Nanoparticles: From Synthesis to Functional Systems. Int J Mol Sci 27:2096. https://doi.org/10.3390/ijms27052096

2. Imran Din M, Rafique F, Hussain MS, et al (2019) Recent developments in the synthesis and stability of metal ferrite nanoparticles. Science Progress 102:61–72. https://doi.org/10.1177/0036850419826799

3. Dobák S, Beatrice C, Tsakaloudi V, Fiorillo F (2022) Magnetic Losses in Soft Ferrites. Magnetochemistry 8:60. https://doi.org/10.3390/magnetochemistry8060060

4. Smit J, Wijn HPJ (1959) Ferrites: Physical Properties of Ferrimagnetic Oxides in Relation to Their Technical Applications. Philips Technical Library, Eindhoven

5. Goldman A (2006) Modern Ferrite Technology, 2nd edn. Springer, New York. https://doi.org/10.1007/978-0-387-29413-1

6. Snoek JL (1948) Dispersion and absorption in magnetic ferrites at frequencies above one Mc/s. Physica 14:207–217. https://doi.org/10.1016/0031-8914(48)90038-X
7. Băjenescu T-M (2021) Miniaturisation of Electronic Components and the Problem of Device Overheating. EEA 69:53–58. https://doi.org/10.46904/eea.21.69.2.1108006
8. Shahi P, Heydari A, Modi H, et al (2024) Maximizing Cooling Potential: A Step-by-Step Guide to Commissioning Liquid-Cooled Data Centers. IEEE, pp 1–12
9. Zhang X, Liu J, Shi L, Wen X (2025) Overview of Single-phase Immersion Liquid Cooling Technology. IJE 7:35–37. https://doi.org/10.54097/dhmrxm38
10. Heydari A, Radmard V, Eslami B, et al (2022) Liquid to Air Cooling for High Heat Density Liquid Cooled Data Centers. American Society Of Mechanical Engineers
11. Chen C, Mithani N, Jin T, Guo A (2022) Liquid Cooling Practice on Meta's AI Training Platform. American Society Of Mechanical Engineers
12. Mukatash W, Kabbani H, Massalt JM, et al (2024) Cooling High Power Dissipating Artificial Intelligence (AI) Chips Using Refrigerant. JECTC 13:35–49. https://doi.org/10.4236/jectc.2024.132002
13. Vilarrubí M (2024) Perspective Chapter: Smart Liquid Cooling Solutions for Advanced Microelectronic Systems. IntechOpen
14. Kuta M, Matuszewska D, Wójcik TM (2019) Maximization of performance of a PCM – based thermal energy storage systems. EPJ Web Conf 213:02049. https://doi.org/10.1051/epjconf/201921302049
15. Ali SA, Habib K, Younas M, et al (2024) Advancements in Thermal Energy Storage: A Review of Material Innovations and Strategic Approaches for Phase Change Materials. Energy Fuels 38:19336–19392. https://doi.org/10.1021/acs.energyfuels.4c03634
16. Prasad NVK, Naidu KCB, Basha DB (2024) Phase Change Materials for Thermal Energy Storage: A Concise Review. NANO 19:. https://doi.org/10.1142/s179329202430010x
17. Muhabie AA, Mengesha WG, Yang X (2026) Advances in Phase Change Materials for Thermal Energy Storage and Management: Challenges and Enhancement Strategies. ACS Omega 11:. https://doi.org/10.1021/acsomega.5c06952
18. Gajghate SS, Noor MM, Pal S, et al (2025) Role of composite PCM material in thermal energy storage application: A comprehensive review. J Phys: Conf Ser 3076:012018. https://doi.org/10.1088/1742-6596/3076/1/012018
19. Abdullah M, Obayedullah M, Musfika SA (2025) Recent Advances in Phase Change Energy Storage Materials: Developments and Applications. International Journal of Energy Research 2025:. https://doi.org/10.1155/er/6668430
20. Amberkar T, Mahanwar P (2022) Phase Change Material Nanocomposites for Thermal Energy Storage Applications. MDPI, p 8
21. Qin B, Zhao L-D (2023) Progress and Challenges for Thermoelectric Cooling: From Materials and Devices to Manifold Applications. MatLab 2:. https://doi.org/10.54227/mlab.20230032
22. Gong X, Qian R, Xue H, et al (2021) Progress of microscopic thermoelectric effects studied by micro- and nano-thermometric techniques. Front Phys 17:. https://doi.org/10.1007/s11467-021-1101-x
23. Peng X, Lei H, Chen J, Liu Y (2025) Novel Hybrid Electronic-Ionic-Type Thermoelectric Device with Enhanced Performance by Using Steel Wool and $[Fe(CN)_6]^{4-}$/$[Fe(CN)_6]^{3-}$ Ion Solution. ACS Sustainable Chem Eng 13:21067–21079. https://doi.org/10.1021/acssuschemeng.5c07379

24. Qin Y, Qin B, Wang D, et al (2022) Solid-state cooling: thermoelectrics. Energy Environ Sci 15:4527–4541. https://doi.org/10.1039/d2ee02408j
25. Lucia U, Grisolia G (2024) Magnetocaloric Refrigeration in the Context of Sustainability: A Review of Thermodynamic Bases, the State of the Art, and Future Prospects. Energies 17:3585. https://doi.org/10.3390/en17143585
26. Bekemeier S, Blum M, Caron L, et al (2025) Fostering Innovation: Streamlining Magnetocaloric Materials Research by Digitalization. arXiv (Cornell University)
27. Gottschall T, Skokov KP, Fries M, et al (2019) Magnetic Refrigeration: Making a Cool Choice: The Materials Library of Magnetic Refrigeration (Adv. Energy Mater. 34/2019). Advanced Energy Materials 9:1970130. https://doi.org/10.1002/aenm.201970130
28. Greco A, Farina AR, Masselli C (2021) Caloric Solid-State Magnetocaloric Cooling: Physical Phenomenon, Thermodynamic Cycles and Materials. TI-IJES 65:58–66. https://doi.org/10.18280/ti-ijes.650109
29. Meduri S, Challa K, Ponangi BR (2024) Magnetic Refrigeration at Room Temperature: A State-of-the-Art Review. In: SAE technical papers on CD-ROM/SAE technical paper series. Federation University Australia
30. Siroux M (2023) Magnetocaloric Refrigeration. 171–207
31. Naagar M, Chalia S, Wan F, et al (2024) Investigations on temperature-dependent magnetic properties and magnetic thermal stability of magnesium ferrite (MgFe2O4) nanoparticles. Journal of Magnetism and Magnetic Materials 592:171798. https://doi.org/10.1016/j.jmmm.2024.171798
32. Wang FZ (2023) Beyond Memristors: Neuromorphic Computing Using Meminductors. Micromachines 14:486. https://doi.org/10.3390/mi14020486
33. Vepulanont K, Sa-Nguanprang S, Buapoon S, et al (2021) Nickel ferrite ceramics: combustion synthesis, sintering, characterization, and magnetic and electrical properties. Journal of Asian Ceramic Societies 9:639–651. https://doi.org/10.1080/21870764.2021.1907031
34. Ravikumar T, Thirumalaisamy L, Sivaperuman K (2024) Synergistic effect of rGO decoration on ZnFe2O4 nanorods for low concentration detection of ammonia at room temperature with high selectivity and response. Surfaces and Interfaces 53:105076. https://doi.org/10.1016/j.surfin.2024.105076
35. Saraf M, Natarajan K, Gupta AK, et al (2019) Electrochemical energy storage properties of solvothermally driven ZnFe2O4 microspheres. Mater Res Express 6:095534. https://doi.org/10.1088/2053-1591/ab3339
36. Tajik S, Askari MB, Ahmadi SA, et al (2022) Electrochemical Sensor Based on ZnFe2O4/RGO Nanocomposite for Ultrasensitive Detection of Hydrazine in Real Samples. Nanomaterials 12:491. https://doi.org/10.3390/nano12030491
37. Abdulhamid ZM, Lokhande AC, Emwas A-H, et al (2025) Unlocking superior energy storage in ZnFe2O4 nanospheres via advanced electrode design: An integrated experimental and computational approach. Electrochimica Acta 535:146622. https://doi.org/10.1016/j.electacta.2025.146622
38. Guo P, Zhang Y, Han F, et al (2022) Unveiling the Coercivity-Induced Electrocatalytic Oxygen Evolution Activity of Single-Domain CoFe2O4 Nanocrystals under a Magnetic Field. J Phys Chem Lett 13:7476–7482. https://doi.org/10.1021/acs.jpclett.2c01843
39. Ma Y, Xu X, Lu L, et al (2021) Facile synthesis of ultrasmall MnFe2O4 nanoparticles with high saturation magnetization for magnetic resonance imaging. Ceramics International 47:34005–34011. https://doi.org/10.1016/j.ceramint.2021.08.308

40. Rahmayeni R, Azizah N, Stiadi Y, et al (2022) Magnetic Particles Nanorod of ZnO/CuFe2O4 Prepared by Green Synthesized Approach: Structural, Optical and Magnetic Properties, and Photocatalytic Activity. Mat Res 25:. https://doi.org/10.1590/1980-5373-mr-2021-0164
41. Hussain S, Rafiq S, Yousaf MI, et al (2024) Tuning optical, magnetic, and electrical parameters of CuFe2O4 nanoparticles incorporated with GO and ZnO using a facile synthesis. Heliyon 10:e33709. https://doi.org/10.1016/j.heliyon.2024.e33709
42. Sohail Y, Liaquat A, Haq AU, et al (2021) Impedance spectroscopy and investigation of conduction mechanism in reduced graphene/CuFe2O4 nanocomposites. Appl Phys A 127:. https://doi.org/10.1007/s00339-021-04563-0
43. Mishra B, Munisha B, Nanda J, et al (2022) Hydrothermally Synthesized Magnesium doped Zinc Ferrite Nanoparticles: An extensive study on structural, optical, magnetic, and dielectric properties. Materials Chemistry and Physics 292:126791. https://doi.org/10.1016/j.matchemphys.2022.126791
44. Venkatesh D, Ramesh KV (2024) The study of structural, frequency and temperature dependence of electrical and dielectric properties of CuO-substituted Ni-Zn nanocrystalline ferrites for MLCI applications. Philosophical Magazine 104:908–932. https://doi.org/10.1080/14786435.2024.2361014
45. Debnath A, Hossen MS, Auntu RS, Shil SK (2025) High permeability with ultra-soft magnetic behavior of solid state method synthesized Al-substituted Ni-Mg-Zn ferrites for high frequency applications. Surfaces and Interfaces 72:107370. https://doi.org/10.1016/j.surfin.2025.107370
46. Mohapatra PP, Singh HK, Kiran MSRN, Dobbidi P (2022) Co substituted Ni–Zn ferrites with tunable dielectric and magnetic response for high-frequency applications. Ceramics International 48:29217–29228. https://doi.org/10.1016/j.ceramint.2022.05.197
47. Thakur P, Taneja S, Chahar D, et al (2021) Recent advances on synthesis, characterization and high frequency applications of Ni-Zn ferrite nanoparticles. Journal of Magnetism and Magnetic Materials 530:167925. https://doi.org/10.1016/j.jmmm.2021.167925
48. Rahman MI (2023) Design of medium frequency transformer for dual active bridge DC/DC converter. AIP Conference Proceedings, p 040007
49. Somkun S, Sato T, Chunkag V, et al (2021) Performance Comparison of Ferrite and Nanocrystalline Cores for Medium-Frequency Transformer of Dual Active Bridge DC-DC Converter. Energies 14:2407. https://doi.org/10.3390/en14092407
50. Kaman O, Kubániová D, Knížek K, et al (2021) Structure and magnetic state of hydrothermally prepared Mn-Zn ferrite nanoparticles. Journal of Alloys and Compounds 888:161471. https://doi.org/10.1016/j.jallcom.2021.161471
51. Abdollahi M, Manouchehri S, Yousefi MH (2021) A new nano-grain Mn–Zn spinel ferrite smart cores to enhance the efficiency of high-frequency devices. Indian J Phys 96:1405–1411. https://doi.org/10.1007/s12648-021-02088-z
52. Angadi VJ, Manjunatha K, Ayachit NH (2021) Correlation of internal strain and size with electrical and magnetic properties of Ce3+-doped manganese ferrimagnetic nanoparticles. J Mater Sci: Mater Electron 32:9275–9293. https://doi.org/10.1007/s10854-021-05592-4
53. Prakash A, Sagayaraj R, Jayarajan D, et al (2022) Influence of Ce3+ Substitution on Magnetic Properties and Antibacterial Activity of Manganese Ferrite Nanoparticles Synthesized by Coprecipitation Method. Asian J Chem 34:2288–2296. https://doi.org/10.14233/ajchem.2022.23840

54. Sagayaraj R, Jegadheeswari M, Aravazhi S, et al (2020) Structural, Spectroscopic and Magnetic Study of Nanocrystalline Terbium–Nickel Ferrite by Oxalate Co-Precipitation Method. Chemistry Africa 3:955–963. https://doi.org/10.1007/s42250-020-00153-4
55. Agboola PO, Haider S, Shakir I (2022) The impact of rare earth Nd3+ cations on structural, spectral, magnetic and dielectric parameters of NiFe2O4 nanoparticles. Journal of Taibah University for Science 16:392–400. https://doi.org/10.1080/16583655.2022.2059953
56. Khedri H, Gholizadeh A (2019) Experimental comparison of structural, magnetic and elastic properties of M0.3Cu0.2Zn0.5Fe2O4 (M = Cu, Mn, Fe, Co, Ni, Mg) nanoparticles. Appl Phys A 125:. https://doi.org/10.1007/s00339-019-3010-1
57. Dippong T, Levei EA, Cadar O (2022) Investigation of Structural, Morphological and Magnetic Properties of MFe2O4 (M = Co, Ni, Zn, Cu, Mn) Obtained by Thermal Decomposition. IJMS 23:8483. https://doi.org/10.3390/ijms23158483
58. Dippong T, Levei EA, Cadar O (2021) Recent Advances in Synthesis and Applications of MFe2O4 (M = Co, Cu, Mn, Ni, Zn) Nanoparticles. Nanomaterials 11:1560. https://doi.org/10.3390/nano11061560
59. Sanchez-Lievanos KR, Stair JL, Knowles KE (2021) Cation Distribution in Spinel Ferrite Nanocrystals: Characterization, Impact on their Physical Properties, and Opportunities for Synthetic Control. Inorg Chem 60:4291–4305. https://doi.org/10.1021/acs.inorgchem.1c00040
60. Zeng X, Hou Z, Ju J, et al (2022) The Cation Distributions of Zn-doped Normal Spinel MgFe2O4 Ferrite and Its Magnetic Properties. Materials 15:2422. https://doi.org/10.3390/ma15072422
61. Zhang Q, Tian W, Matsuda M, et al (2021) Structural magnetic ordering process and the magnetic excitations in spinel $FeMn_2O_4$. Acta Cryst A 77:a140. https://doi.org/10.1107/s0108767321098597
62. Wang X, Musicó BL, Kons C, et al (2022) Local cation order and ferrimagnetism in compositionally complex spinel ferrites. APL Materials 10:121102. https://doi.org/10.1063/5.0123728
63. Manju M, Kaur K (2025) Introduction to Spinel and Inverse Spinel Ferrites. Chapman & Hall/CRC Press, pp 1–15
64. Ouyahia S, Rais A, Bozzo B, et al (2020) Cations distribution by Rietveld refinement and magnetic properties of MgCrxFe2−xO4 spinel ferrites. Appl Phys A 126:. https://doi.org/10.1007/s00339-020-03865-z
65. Kolekar RY, Kapatkar SB, Kakati SS, Mathad SN (2024) Impact of Magnesium on Structural and Morphological Study of Co–Zn Ferrites. Int J Self-Propag High-Temp Synth 33:58–66. https://doi.org/10.3103/s1061386224010047
66. Sagayaraj R, Aravazhi S, Chandrasekaran G (2021) Review on structural and magnetic properties of (Co–Zn) ferrite nanoparticles. Int Nano Lett 11:307–319. https://doi.org/10.1007/s40089-021-00343-z
67. Ingle PA, Kadam SB, Borade RB, et al (2025) Tailoring Structural and Magnetic Properties of Co–Zn Ferrite Nanoparticles via Erbium Substitution. Research Square
68. Sagayaraj R, Aravazhi S, Chandrasekaran G (2021) Microstructure and magnetic properties of Cu0.5Co0.3Mo0.2Fe2O4 ferrite nanoparticles synthesized by coprecipitation method. Appl Phys A 127:. https://doi.org/10.1007/s00339-021-04653-z
69. Sagayaraj R, Aravazhi S, Selva Kumar C, et al (2019) Tuning of ferrites (CoxFe3-xO4) nanoparticles by co-precipitation technique. SN Appl Sci 1:. https://doi.org/10.1007/s42452-019-0244-7

70. Sagayaraj R, Aravazhi S, Chandrasekaran G (2019) Effect of Zinc Content on Structural, Functional, Morphological, Resonance, Thermal and Magnetic Properties of Co1−xZnxFe2O4/PVP Nanocomposites. J Inorg Organomet Polym 29:2252–2261. https://doi.org/10.1007/s10904-019-01183-3
71. Kulesh N, Permyakov N, Zverev V, et al (2022) Combined Micromagnetic Simulation and Machine Learning Approach to Analysis of Polycrystalline Bilayer With Exchange Bias. IEEE Trans Magn 58:1–5. https://doi.org/10.1109/tmag.2021.3077288
72. Sort J (2025) Beyond storage: The expanding role of magnetism in intelligent computing. APL Materials 13:. https://doi.org/10.1063/5.0283713
73. Zeng X, Liu J, Chu K, et al (2025) Atomic-level cation occupation and magnetic properties of Ce3+-doped ZnFe2O4 spinel ferrite†. RSC Adv 15:20908–20915. https://doi.org/10.1039/d5ra01515d
74. Nayak S, Roy PK, Ghorai S, et al (2025) Effect of thermally-induced cationic redistribution on the structural and magnetic properties of Cu-substituted zinc ferrite. J Phys: Condens Matter 37:155802. https://doi.org/10.1088/1361-648x/adb824
75. Muzzi B, Albino M, Petrecca M, et al (2023) Defect-Engineering by Solvent Mediated Mild Oxidation as a Tool to Induce Exchange Bias in Metal Doped Ferrites. Small Methods 7:e2300647. https://doi.org/10.1002/smtd.202300647
76. Sun Y, Deng X, Zong Y, et al (2021) Cation ratio and oxygen defects for engineering the magnetic transition of monodisperse nonstoichiometric zinc ferrite nanoparticles. Sci China Mater 64:2017–2028. https://doi.org/10.1007/s40843-020-1592-y
77. Thakur A, Manhas A, Singh V, et al (2025) Review on Fabrication Methods with the Tailoring of Applications of Magnetic Nanoparticles Based on Their Physical Parameters. Integrated Ferroelectrics 241:334–359. https://doi.org/10.1080/10584587.2025.2482434
78. Honecker D, Disch S (2021) Revealing Magnetic Morphologies and Spin Disorder in Ferrite Nanoparticles using polarized SANS. In: Underline Science Inc.
79. Ntallis N, Trohidou KN (2023) Effect of Organic Coating Variation on the Electric and Magnetic Behavior of Ferrite Nanoparticles. ACS Phys Chem Au 3:532–539. https://doi.org/10.1021/acsphyschemau.3c00026
80. Zhang L, Alifu N, Lan Z, et al (2023) Surface modification of multifunctional ferrite magnetic nanoparticles and progress in biomedicine. Sheng wu yi xue gong cheng xue za zhi = Journal of biomedical engineering = Shengwu yixue gongchengxue zazhi 40:378–383. https://doi.org/10.7507/1001-5515.202209056
81. Dhyani R, Joshi A, Sahoo VN, Singh JP (2024) Physical Property Variation of Ferrite Nanoparticles under Heavy Ion Irradiation. Prabha Materials Science Letters 3:1–28. https://doi.org/10.33889/pmsl.2024.3.1.001
82. Andalib P (2019) Enhanced thermal management in high frequency ferrite-based inductor cores via grain boundary nanoengineering strategies. Northeastern University Library
83. Wu G, Yu Z, Guo R, et al (2023) Effects of magnetic domain morphology on the magnetic spectrum and high-frequency core losses of MnZn ferrites. J Am Ceram Soc 107:1117–1126. https://doi.org/10.1111/jace.19519
84. Karaagac O, Hasirci, H C (2024) Optimum Saturation Magnetization of Superparamagnetic Iron Oxide Nanoparticles for Versatile Applications. Acta Phys Pol A 146:154–164. https://doi.org/10.12693/aphyspola.146.154

85. Saladino GM, Kakadiya R, Ansari SR, et al (2023) Magnetoresponsive fluorescent core–shell nanoclusters for biomedical applications†. Nanoscale Adv 5:1323–1330. https://doi.org/10.1039/d2na00887d
86. Fahim YA, Hasani IW, Mahmoud Ragab W (2025) Promising biomedical applications using superparamagnetic nanoparticles. Eur J Med Res 30:441. https://doi.org/10.1186/s40001-025-02696-z
87. Zhang R, Qin C, Bala H, et al (2023) Recent Progress in Spinel Ferrite (MFe2O4) Chemiresistive Based Gas Sensors. Nanomaterials 13:2188. https://doi.org/10.3390/nano13152188
88. Fokin N, Grothe T, Mamun A, et al (2020) Magnetic Properties of Electrospun Magnetic Nanofiber Mats after Stabilization and Carbonization. Materials 13:1552. https://doi.org/10.3390/ma13071552
89. Guarino V, Iannotti V, Ausanio G, et al (2019) Elastomagnetic nanofiber wires by magnetic field assisted electrospinning. Express Polym Lett 13:419–428. https://doi.org/10.3144/expresspolymlett.2019.35
90. Blachowicz T, Steblinski P, Ehrmann A (2023) Influence of Physical Symmetries on the Magnetization Dynamics in Magnetic Fibers. Symmetry 15:234. https://doi.org/10.3390/sym15010234
91. Ameen S, Akhtar M, Kong I (2024) Advances in Nanofiber Research - Properties and Uses. IntechOpen
92. Dai J, Cheng C, Li Z, Feng W (2019) The relationship between magnetic properties and morphology of nanocomposites. Mater Res Express 6:086116. https://doi.org/10.1088/2053-1591/ab24aa
93. Yu Z, Ji N, Li X, et al (2022) Kinetics Driven by Hollow Nanoreactors: An Opportunity for Controllable Catalysis. Angew Chem Int Ed 62:e202213612. https://doi.org/10.1002/anie.202213612
94. Li Y, Liu J, Mcclements DJ, et al (2024) Recent Advances in Hollow Nanostructures: Synthesis Methods, Structural Characteristics, and Applications in Food and Biomedicine. J Agric Food Chem 72:20241–20260. https://doi.org/10.1021/acs.jafc.4c05910
95. Zhu M, Cheng Y, Luo Q, et al (2021) A review of synthetic approaches to hollow nanostructures. Mater Chem Front 5:2552–2587. https://doi.org/10.1039/d0qm00879f
96. Sun L, Shi Z, Liang L, et al (2022) Concurrently Achieving High Discharged Energy Density and Efficiency in Composites by Introducing Ultralow Loadings of Core-Shell Structured Graphene@TiO2 Nanoboxes. ACS Appl Mater Interfaces 14:29292–29301. https://doi.org/10.1021/acsami.2c07229
97. Xu Y, Liu J, Wang Y, et al (2025) Synthesis and investigation of Cu@few-layer graphene shell composites with exceptional conductivity and chemical stability. Dalton Trans 54:15849–15855. https://doi.org/10.1039/d5dt01293g
98. Shao Q, Wang P, Liu S, Huang X (2019) Advanced engineering of core/shell nanostructures for electrochemical carbon dioxide reduction. J Mater Chem A 7:20478–20493. https://doi.org/10.1039/c9ta07016h
99. Tian Y, Hu X, Wang Y, et al (2019) Fe_2O_3 Nanoparticles Decorated on Graphene-Carbon Nanotubes Conductive Networks for Boosting the Energy Density of All-Solid-State Asymmetric Supercapacitor. ACS Sustainable Chem Eng 7:9211–9219. https://doi.org/10.1021/acssuschemeng.8b06857

100. Jones CF, Resina L, Ferreira FC, et al (2024) Conductive Core–Shell Nanoparticles: Synthesis and Applications. J Phys Chem C 128:11083–11100. https://doi.org/10.1021/acs.jpcc.4c02012
101. Li H, Tang C, An X, et al (2022) Fe_3O_4 Nanoparticles Enhanced Amorphous Ferric Silicate/Reduced Graphene Oxide for High-Performance Lithium-Ion Storage. Adv Materials Inter 9:2201192. https://doi.org/10.1002/admi.202201192
102. Asha A, Juglan KC, Jain A (2024) A review on magnetic properties, synthesis, characterization, and applications of Mn-Ni Fe2O4 ferrites. AIP Conference Proceedings, p 030127
103. Suraj KS, Eivari HA, Tatara G, Assadi MHN (2024) Tripling magnetite's thermoelectric figure of merit with rare earth doping. J Mater Chem C 12:19212–19218. https://doi.org/10.1039/d4tc03153a
104. Sharma D, Bala K (2025) Magnetic Properties of Spinel and Inverse Spinel Ferrites. Chapman & Hall/CRC Press, pp 56–69
105. Li H, Li W, Robichaud J, Djaoued Y (2025) Magnetic Spinel Ferrite Nanomaterials: Fabrication and Application. IntechOpen
106. Hölscher J, Petrecca M, Albino M, et al (2020) Magnetic Property Enhancement of Spinel Mn-Zn Ferrite through Atomic Structure Control. Inorg Chem 59:11184–11192. https://doi.org/10.1021/acs.inorgchem.0c01809
107. Zákutná D, Nižňanský D, Barnsley LC, et al (2020) Field Dependence of Magnetic Disorder in Nanoparticles. Phys Rev X 10:. https://doi.org/10.1103/physrevx.10.031019
108. Patil SB, Davari AJ, Patil DR, Patil RP (2020) Microstructure and Magnetic Properties of Ni-Mg-Zn-Co Ferrites. Macromolecular Symposia 393:2000179. https://doi.org/10.1002/masy.202000179
109. Islam MJ, Jhahan M, Khatun MT, et al (2021) Influence of Mg substitution on structural, magnetic and electrical properties of Zn-Cu ferrites. J Mater Sci: Mater Electron 32:26173–26180. https://doi.org/10.1007/s10854-021-06617-8
110. Wu T, Wang C, Ma Z, et al (2026) Optimizing magnetic and electrical properties of MnZn ferrites via spatially engineered Ni distribution. Journal of Advanced Ceramics 15:9221240. https://doi.org/10.26599/jac.2026.9221240
111. Thakur P, Kumari S, Singh S, et al (2023) Mg-Zn Ferrite Nanoparticles: A Brief Review on Synthesis, Characterizations, and Applications. ChemBioEng Reviews 10:711–736. https://doi.org/10.1002/cben.202200063
112. Wu X-H, Tao Z-X, Li L-Z, et al (2020) Crystal structure and enhanced magneto-electric properties of cobalt-substituted nickel–zinc ferrite. J Mater Sci: Mater Electron 31:20277–20284. https://doi.org/10.1007/s10854-020-04547-5
113. Li Y, Sun J, Li S-L, Leão-Santos M (2021) A paradigm shift in magnetic data interpretation: Increased value through magnetization inversions. The Leading Edge 40:89–98. https://doi.org/10.1190/tle40020089.1
114. Liu J, Davis C, Yue S, et al (2025) Scalar permeability microstructure model considering crystallographic texture and grain size for magnetic evaluation of anisotropy in steel. Acta Materialia 289:120863. https://doi.org/10.1016/j.actamat.2025.120863
115. Choudhary AK, Kini A, Hohs D, et al (2023) Machine learning-based Curie temperature prediction for magnetic 14:2:1 phases. AIP Advances 13:035112. https://doi.org/10.1063/5.0116650

116. Arale Brännvall M, Persson G, Casillas-Trujillo L, et al (2024) Predicting the Curie temperature of magnetic materials with automated calculations across chemistries and structures. Phys Rev Materials 8:. https://doi.org/10.1103/physrevmaterials.8.114417
117. Skomski R, Coey JMD (2019) Anisotropy and coercivity. Routledge, pp 124–206
118. Poon K, Kumar J, Saraswathy J, et al (2025) Anisotropic Magnetic Nanoparticles. 79–101
119. Ma Z, Mohapatra J, Wei K, et al (2021) Magnetic Nanoparticles: Synthesis, Anisotropy, and Applications. Chem Rev 123:3904–3943. https://doi.org/10.1021/acs.chemrev.1c00860
120. De Campos MF (2024) The Concept of Heat and the Hysteresis Loop: The Evolution of the Losses Models. Acta Phys Pol A 146:34–40. https://doi.org/10.12693/aphyspola.146.34
121. Renuka Balakrishna A (2024) Rethinking hysteresis in magnetic materials. MRS Communications 14:835–845. https://doi.org/10.1557/s43579-024-00624-6
122. Deng J, Wang W, Ning Z, et al (2024) High-Frequency Core Loss Modeling Based on Knowledge-Aware Artificial Neural Network. IEEE Trans Power Electron 39:1968–1973. https://doi.org/10.1109/tpel.2023.3332025
123. Jacobs S, Rens J (2025) The impact of the physical, electrical and magnetic properties of ferromagnetic materials on their excess loss. AIP Advances 15:. https://doi.org/10.1063/9.0000867
124. Bertolini V, Scorretti R, Faba A, Cardelli E (2025) Fast Estimation of Eddy Current Power Losses in Soft Ferrites Rings. IEEE Access 13:198228–198240. https://doi.org/10.1109/access.2025.3634470
125. Shen X, Zuo Y, Kong J, Martinez W (2024) Artificial Intelligence Applications in High-Frequency Magnetic Components Design for Power Electronics Systems: An Overview. IEEE Trans Power Electron 39:8478–8496. https://doi.org/10.1109/tpel.2024.3381431
126. Sapkota DB, Neupane P, Joshi M, Khan S (2024) Deep learning model for enhanced power loss prediction in the frequency domain for magnetic materials. IET Power Electronics 19:. https://doi.org/10.1049/pel2.12704
127. Liu R, Li L (2020) Analytical Prediction Model of Energy Losses in Soft Magnetic Materials Over Broadband Frequency Range. IEEE Trans Power Electron 36:2009–2017. https://doi.org/10.1109/tpel.2020.3009283
128. Wang H, Brown A, Wu Y, et al (2025) Automatic Loss Measurement System for MHz Magnetics Using High-Frequency Conditioning Circuits. IEEE, pp 1–7
129. Naoe M (2024) Magnetic Materials for High-Frequency Applications. T IEE Japan 144:186–193. https://doi.org/10.1541/ieejfms.144.186
130. Kumar S, Singh RR (2023) Ferrite Nanoparticles for Telecommunication Application. Springer Nature Singapore, pp 95–112
131. Han M (2020) High-Frequency Permeability of Fe-Based Nanostructured Materials. IntechOpen
132. Sun Z, Zhang P, Liu W, He W (2025) Fundamentals of Materials Science
133. Martins S, De Rojas J, Tan Z, et al (2022) Dynamic electric-field-induced magnetic effects in cobalt oxide thin films: towards magneto-ionic synapses. Nanoscale 14:842–852. https://doi.org/10.1039/d1nr06210g
134. Sun S-J, Baczewski LT, Wojnar P, et al (2020) Theoretical model investigating the magnetic properties of cobalt-doped ZnO. J Phys: Condens Matter 32:225801. https://doi.org/10.1088/1361-648x/ab6e8c
135. Zacharias P, Friebe J, Dick CP (2024) Metallic magnetic materials. IET, pp 25–43

136. Jang S, Kawsar F, Min C (2024) Thermal Characterization of AI Applications on AI Accelerators-equipped Microcontrollers. Association for Computing Machinery, pp 17–22
137. Knisley T (2025) Materials Innovation for Thermal Interfaces: Unlocking AI Compute Efficiency. Meet Abstr MA2025-02:3611. https://doi.org/10.1149/ma2025-02313611mtgabs
138. Kaur B, Kaushal G, Rana S, et al (2022) Magnetic Ferrites: A Brief Review About Substation on Electric and Magnetic Properties. ECS Trans 107:9093–9101. https://doi.org/10.1149/10701.9093ecst
139. Amato A, Becci A, Bollero A, et al (2023) Life CycleAssessment of Rare Earth Elements-FreePermanent Magnet Alternatives: Sintered Ferrite and Mn–Al–C. ACS Sustainable Chem Eng 11:13374–13386. https://doi.org/10.1021/acssuschemeng.3c02984
140. Gupta M, Das A, Das D, et al (2020) Chemical Synthesis of Rare Earth (La, Gd) Doped Cobalt Ferrite and a Comparative Analysis of Their Magnetic Properties. j nanosci nanotechnol 20:5239–5245. https://doi.org/10.1166/jnn.2020.18528
141. Nabih A, Li Q (2024) A Method to Embed Resonant Inductor Into PCB Matrix Transformer for High-Density Resonant Converters. IEEE Trans Power Electron 39:2385–2400. https://doi.org/10.1109/tpel.2023.3330974
142. Brown A, Ng E, Hanson A (2024) Magnetic material selection for power inductors and transformers. IET, pp 107–128
143. Shimizu T (2019) Iron Loss of the Inductors. Springer Singapore, pp 391–405
144. Shimizu T (2023) Passive Components for Advancement of Power Electronics. IEEE, pp 1–2
145. Zunino S, Sforna M, Ferrari F (2023) Magnetic materials for power transformers. IET, pp 7–89
146. Li C, Cheng M, Qin W, et al (2025) Core Loss Model for Nonsinusoidal Excitations Based on Vector Magnetic Circuit Theory. IEEE Trans Power Electron 40:16926–16936. https://doi.org/10.1109/tpel.2025.3588673
147. Qian D, Cheng M, Qin W, et al (2024) Analysis and Design of High Frequency Cores Based on Vector Magnetic Circuit Theory. IEEE, pp 22–30
148. Sun J, Ren J, Li J, Huang Y (2023) Measurement and Analysis of Magnetic Properties of Permalloy for Magnetic Shielding Devices under Different Temperature Environments. Materials 16:3253. https://doi.org/10.3390/ma16083253
149. Paplham TW, Leary AM, Ohodnicki PR (2025) Extreme Temperature Permeability Engineered Soft Magnetics. IEEE, pp 2516–2520
150. Wu X, Wu W, Zhou K, et al (2013) Magnetic Nanocrystalline Mg0.5Zn0.5Fe2O4: Preparation, Morphology Evolution, and Kinetics of Thermal Decomposition of Precursor. J Supercond Nov Magn 27:511–518. https://doi.org/10.1007/s10948-013-2297-y
151. Balamurugan S, Ragasree R, Brightlin BC, Raja TSG (2021) Magnetic Properties of Mechano-Thermally Processed Nanocrystalline MgFe2O4 Spinel Materials. J Clust Sci 33:547–555. https://doi.org/10.1007/s10876-021-01998-6
152. Akhter S, Hoque SM, Hakim MA (2019) Effect of sintering temperature on structural and magnetic properties of bulk Mg-ferrites. International Journal of Materials Research 110:979–984. https://doi.org/10.3139/146.111828
153. Jadhav SS, Jadhav SP, Ramshetti RS, et al (2021) Ferrimagnetic to paramagnetic transition and dielectric relaxation in Ni1-xZnxFe2O4 ferrites. Cerâmica 67:139–144. https://doi.org/10.1590/0366-69132021673823028

154. Zaspalis S, Kogias G, Zaspalis V (2024) The Effect of Sintering Temperature on the Densification and Magnetic Performance of NiCuZn-Ferrites (CuO: 0-6 wt.%). Materials 17:2293. https://doi.org/10.3390/ma17102293
155. Sharma US, Shah R (2018) Investigation of electronic and magnetic properties of Ni0.5Cu0.5Fe2O4: theoretical and experimental. AIP Conference Proceedings, p 030091
156. Zhu JF, Chen MN, Ke SD, Feng SJ (2019) Magnetic properties of indium doped Ni0.4Zn0.6InxFe2−xO4. Mater Res Express 6:116127. https://doi.org/10.1088/2053-1591/ab50b0
157. Lathiya P, Wang J (2021) Enhancement in magnetic permeability of Ni-Co-Zn ferrites using CuO doping for RF and microwave devices. J Am Ceram Soc 105:2678–2689. https://doi.org/10.1111/jace.18253
158. Nazari N, Golzan MM, Mabhouti K (2025) Evaluating eddy current behavior and magnetic loss in pure and Mn/Zn-doped NiFe2O4 spinel ferrites. Sci Rep 15:25169. https://doi.org/10.1038/s41598-025-11393-0
159. Bibi M, Sadiq M, Rizk MA, et al (2023) Tuning the Magnetic and Catalytic Properties of Manganese Ferrite through Zn2+ Doping: Gas Phase Oxidation of Octanol. Catalysts 13:1473. https://doi.org/10.3390/catal13121473
160. Li J, Zhao Q, Bandaru S, et al (2025) Tailoring Structural, Electronic, and Magnetic Properties of Fe_3O_4 and MnZn-Ferrites through Metal/Non-metal Doping: A DFT+U Study. J Phys Chem C 129:12124–12135. https://doi.org/10.1021/acs.jpcc.5c02045
161. Thakur P, Taneja S, Sindhu D, et al (2020) Manganese Zinc Ferrites: a Short Review on Synthesis and Characterization. J Supercond Nov Magn 33:1569–1584. https://doi.org/10.1007/s10948-020-05489-z
162. Rengasamy S, Kumar AR (2025) Unlocking the Potential of Manganese Ferrite: A Comprehensive Review of its Applications. ChemistrySelect 10:. https://doi.org/10.1002/slct.202503628
163. Vishwarup R, Kulkarni AB, Manohara SR, Mathad SN (2021) Influence of Zinc Doped Structural Properties of Nano-$MgFe_2O_4$ Ferrites Synthesized by Co-Precipitation Method. Macromolecular Symposia 400:2100088. https://doi.org/10.1002/masy.202100088
164. Zaspalis S, Kogias G, Zaspalis V, et al (2025) Development of NiZn Ferrites Doped with Co for Low Power Losses at High Frequencies (10 MHz) and High Temperatures (>80 °C). Magnetochemistry 11:44. https://doi.org/10.3390/magnetochemistry11050044
165. Jiang S-P, Yuan C-L, Liu W, et al (2025) BaCo0.06Bi0.94O3-Doped NiZn Ferrites for High Frequency Low Loss Current Sensors: LTCC Sintering and Magnetic Properties. Sensors 25:2731. https://doi.org/10.3390/s25092731
166. Li Y, Zhang Z, Yu J, et al (2024) High-Frequency Modeling and Analysis of Single-Layer NiZn Ferrite Inductors for EMI Filtering in Power Electronics Applications. Energies 17:5657. https://doi.org/10.3390/en17225657
167. Dahiya P, Malik R, Hooda A, Khasa S (2025) Property Tuning in Ni-Zn Ferrites via Zn Substitution: A Step Toward Functional Ferrite Materials. JOM 77:8200–8210. https://doi.org/10.1007/s11837-025-07555-0
168. Wang N, Ying Y, Zheng J, et al (2021) Development of Mn-Zn power ferrite with low losses over a broad temperature range for applications in the high frequency region of 0.5-3 MHz. Ceramics International 47:21425–21432. https://doi.org/10.1016/j.ceramint.2021.04.152
169. Ruwisch K, Pohlmann T, Bertram F, et al (2022) Real-Time Monitoring the Growth of Epitaxial CoxFe3\\u2212xO4 Ultrathin Films on Nb-Doped SrTiO3(001) via Reactive Molecular

Beam Epitaxy by Means of Operando HAXPES. Materials 15:2377. https://doi.org/10.3390/ma15072377
170. Faizan M, Qian Z, Zhu H, et al (2025) Emerging Ferroelectric Materials for High-Performance Next-Generation Memory Devices. ACS Appl Electron Mater 7:7473–7502. https://doi.org/10.1021/acsaelm.5c01058
171. Zheng Y, Xu H, Li Z, et al (2025) Artificial Intelligence-Driven Approaches in Semiconductor Research. Advanced Materials 37:e2504378. https://doi.org/10.1002/adma.202504378
172. Khan A, Yoo HJ, Shinde SL, Ravindran PV (2021) Materials opportunities for low-energy computing. MRS Bulletin 46:925–929. https://doi.org/10.1557/s43577-021-00207-z
173. Kim G, Seok H, Son S, et al (2026) Thermal Expansion-Engineered Ferroelectric Transistor Arrays for Scalable Edge AI Computing. ACS Nano 20:4057–4067. https://doi.org/10.1021/acsnano.5c14095
174. Zou H, Hu Y, Zhu X, et al (2019) Rare Earth Doping Brings Thermal Stability Improvement in Zn0.15Sb0.85 Alloy for Phase Change Memory Application. Journal of Elec Materi 48:4362–4367. https://doi.org/10.1007/s11664-019-07219-1
175. Fuselier M, Bair L, Kulkarni D, et al (2024) Advancing AI with Energy-Efficient Architectures: Innovations in Fab Process, Packaging, and System Integration. IEEE, pp 1–6
176. Kalra N, Tudu JT (2024) AI-Driven Power Gating for Enhanced Energy Efficiency in Superscalar Processors. IEEE, pp 155–156
177. Wood M (2024) High Current Density Power Modules Mitigate the Environmental Impact of Power-Intensive GenAI. IEEE Power Electron Mag 11:20–25. https://doi.org/10.1109/mpel.2024.3398448
178. Nagar P, Boruah S, Bhoi AK, et al (2024) Emerging VLSI Technologies for High performance AI and ML Applications. IEEE, pp 1–5
179. Kar M, Silberman J, Venkataramani S, et al (2024) 14.1 A Software-Assisted Peak Current Regulation Scheme to Improve Power-Limited Inference Performance in a 5nm AI SoC. IEEE, pp 254–256
180. Padmapriya S, S S, S DM, et al (2024) Sustainable Low-Power ALU and Multiplexer based AI Accelerator Design and Optimization Using Cadence. IEEE, pp 472–477
181. Pandey P (2021) Embracing Low-Power Systems with Improvement in Security and Energy-Efficiency. https://doi.org/10.26076/1a04-d500
182. Deprospo B, Bergman E (2025) Saras eVR STile - Demonstration of Next Generation Integrated Passives for Next Generation AI & HPC Power Delivery Network Designs. IMAPSource Proceedings 2025:. https://doi.org/10.4071/001c.147194
183. Chi Q, Ma T, Dong J, Cui Y, Zhang Y, Zhang C, Xu S, Wang X, Lei Q (2017) Enhanced thermal conductivity and dielectric properties of iron oxide/polyethylene nanocomposites induced by a magnetic field. Sci Rep 7:3072. https://doi.org/10.1038/s41598-017-03273-z
184. Gavili A, Zabihi F, Isfahani TD, Sabbaghzadeh J (2012) The thermal conductivity of water base ferrofluids under magnetic field. Exp Therm Fluid Sci 41:94–98. https://doi.org/10.1016/j.expthermflusci.2012.03.016
185. Elmouloua, S., Hadouch, Y., Ayadh, S. et al. Enhancement in Magnetic and Magnetocaloric Properties of $CoFe_2O_4$ Nanofibers at Lower Temperatures. J. Electron. Mater. 53, 7794–7804 (2024). https://doi.org/10.1007/s11664-024-11459-1